ELSEVIER

RESEARCH: Review

Mid-infrared photonics and optoelectronics in 2D materials

Guozhen Liang [1], Xuechao Yu [1], Xiaonan Hu [1], Bo Qiang [1], Chongwu Wang [1], Qi Jie Wang [1,2,*]

[1] Center for Optoelectronics and Biophotonics, School of Electrical and Electronic Engineering & The Photonics Institute, Nanyang Technological University, 50 Nanyang Avenue, 639798 Singapore, Singapore
[2] Center for Disruptive Photonic Technology, School of Physical and Mathematical Sciences, Nanyang Technological University, 50 Nanyang Avenue, 639798 Singapore, Singapore

With intriguing properties that are different from the conventional bulk materials, two-dimensional (2D) materials have attracted numerous and widespread research interests, including its applications in photonics and optoelectronics. Devices based on 2D materials have been demonstrated in a wide spectral range, from the ultraviolet to the terahertz, and the microwave wavelength range. The mid-infrared (MIR) region (about 2–20 μm) bears a particular scientific and technological significance because, for instance, many molecules have their spectral fingerprints and there are atmosphere transparent windows in this region. Nevertheless, the MIR region remains underdeveloped compared to the visible and the near-infrared telecommunication regimes, mainly due to the lack of suitable materials, such as narrow bandgap materials, and proper photonic designs for building high performance optoelectronic devices in this wavelength regime. Therefore, researchers have been exploring the possibility and opportunity of 2D materials to fill up the gap. Here, we review the key recent developments of 2D materials in the MIR photonic and optoelectronic applications, including photodetection, light modulation, surface plasmon polaritons, phonon polaritons, and their nonlinearities and provide an outlook on the challenges and opportunities that lie ahead for MIR optoelectronic research fields with 2D materials.

Keywords: 2D materials; Mid-infrared; Photonics; Optoelectronics

Introduction

Mid-infrared (MIR) spectral region, hereafter defined as the 2–20 μm wavelength range, hosts both scientific and technological interests. For instance, many molecules have strong and unique spectral fingerprints in this region and there are two atmosphere transparent windows (at ~3–5 μm and ~8–12 μm, respectively). Therefore, MIR photonic and optoelectronic devices are potentially promising for a breath of various applications such as gas sensing, environmental monitoring, communication, defense, security, industrial process control, and medicine, etc [1–3]. However, the MIR technologies remain less mature as compared to the technologies in the other frequency regimes, with a dearth in both passive and active photonic components. MIR optoelectronic devices, including light sources, modulators, photodetectors, etc, often require materials with narrow bandgap, which unfortunately only exists in few materials. As an example for MIR detectors, HgCdTe (MCT) is one of such materials widely used [4]. It is the ternary alloy of CdTe (~1.5 eV bandgap) and HgTe (zero bandgap), and the ratio between the two substances determines the bandgap of the MCT between 0 and 1.5 eV, covering the whole MIR range. Nevertheless, MCT detectors nor-

* Corresponding author.
E-mail address: Wang, Q.J. (qjwang@ntu.edu.sg)

https://doi.org/10.1016/j.mattod.2021.09.021

mally require cryogenic cooling and have limited operation speed (at the MHz level). Instead of using direct bandgap material, MIR detectors based on intersubband transitions in quantum wells (QWs), heterojunction superlattice or quantum dots (QDs) have shown great potentials in the long-wavelength regime [5–8]. Quantum well/dot infrared photodetectors have been under rapid development, but most of them are still subject to low-temperature operation, limited by their high dark current although some room-temperature operation has been demonstrated at certain wavelengths [7,8].

Since the discovery of graphene in 2004, two-dimensional (2D) materials have drawn intense research interests due to their unique and intriguing electrical and optical properties [9]. Recent investigations also revealed that some of the 2D materials hold great promise for MIR photonics and optoelectronics. Graphene features a linear cone-like band structure, which enables an ultrabroadband optical absorption, ranging from the visible to the far-infrared [10]. Beyond graphene, various 2D materials such as black phosphorene, transition metal chalcogenides (TMDs), and so on, also have been widely employed in MIR optoelectronic devices [11]. Compared with the traditional bulk MIR optoelectronic materials such as HgCdTe, 2D materials exhibit exceptional properties such as ultrafast speed and broadband response bandwidth [12,13], together with the flexibility of integration into 2D heterostructures [14] and CMOS compatible platforms. A plethora of photonic and optoelectronic devices based on 2D materials have been demonstrated recently, including photodetectors, modulators, polaritonic devices, and nonlinear optical devices, attracting tremendous interests from various research fields including but not limited to material science, photonics, applied physics, and engineering. In this review, we will review these four types of devices and the corresponding 2D materials that are required to achieve the desired functions separately in the following parts of this review.

Photodetector

The unique properties of 2D materials mentioned above enable their applications in ultrafast and ultrasensitive photodetection in a broadband wavelength range, thanks to their ability in converting MIR irradiation to electrical signals [15]. The figure-of-merits of photodetectors mainly include responsivity, response time and bandwidth, noise equivalent power, detectivity, dynamic range and operation bandwidth. In this section, the recent research progress of MIR photodetectors based on graphene and other 2D materials will be overviewed, followed by a discussion on the challenges and limitations.

The operation mechanisms of a detector in the MIR include the photovoltaic (PV) effect, thermoelectric (TE) effect, bolometric effect, photogating effect, etc. In the PV effect, photovoltage/photocurrent generation is based on the separation of photoexcited electron-hole (e-h) pairs by a built-in electrical field at the electrodes or materials with different doping levels [16]. Materials with efficient MIR absorption and photocarrier generation/separation are required in this scenario. In the TE effect, a thermoelectric voltage is generated by a photoinduced temperature gradient. The bolometric effect is based on a change of material's resistance by light-induced heating. The change in channel resistance can be monitored with the presence of an external bias voltage. For this operation mechanism, it is normally required materials possessing high Seebeck coefficient and high temperature coefficient of resistance, etc. The photogating effect relies on injection or depletion of charge carriers in a material, and the change in the carrier concentration can be detected by applying external electrical bias [17] to measure the change of the resistance or conductivity of the material. Different photodetection mechanisms have their own pros and cons. They could be selected based on the availability of suitable high quality 2D materials and the required device performance at different wavelengths for various application scenarios.

MIR photodetectors based on pristine graphene

Traditional graphene-based photodetectors with two identical electrodes have symmetric Schottky barriers formed in the metal-graphene interfaces. The photocurrents generated from both electrodes cancel each other, and thus the net photocurrent in this kind of detector is zero if the two electrodes are illuminated equally and no external bias is applied [18,19]. The photo-thermoelectric effect based on asymmetric electrodes could be used for photocurrent generation enhancement, where the improved responsivity of the graphene photodetectors reported is attributed to the charge separation of the excited electron/hole pairs under built-in bias voltage in the graphene/metal junctions (Fig. 1a). In 2013, the mechanism was systematically investigated, indicating that the photocurrent generation mechanism was dominated by the photovoltaic effect for low doped graphene and by the photo-induced bolometric effect for highly doped graphene [20]. In this type of photodetector, the low absorption of monolayer graphene limits the external quantum efficiency of the device. Dual-gated graphene photodetectors was reported by Gabor et al as shown in Fig. 1b, showing that nonlocal hot carrier transport in graphene dominates the response in photothermal graphene-based detectors [21]. On the other hand, bilayer graphene has also attracted great attention for infrared photodetectors owning to its easier tunability of the bandgap by electrical gating or magnetic field [22,23]. Bolometers made of dual-gated bilayer graphene with tunable bandgap have been demonstrated to exhibit low noise-equivalent power (NEP) and high response speed, which are comparable to the state-of-art commercial MIR bolometers [24].

However, the intrinsic graphene-based detectors have the challenge of low light absorption. Several approaches have been demonstrated to increase light absorption thus the responsivity, including plasmonic enhancement via graphene plasmons, using external plasmonic structures, building optical cavities, or employing waveguides, etc. The Dirac plasmons of graphene can be excited in the MIR region, which can greatly enhance the light absorption by graphene [25–28]. Freitag et al. demonstrated that photoresponse can be increased by about four times induced by the plasmonic effect in optimally designed graphene nanoribbons (GNRs) as indicated in Fig. 1c. Consequently, MIR graphene photodetection was demonstrated by Guo et al as shown in Fig. 1d, where graphene plasmonsic resonators were interconnected by quasi-one-dimensional nanoribbions [29]. Responsivity of 16 mA/W and low noise-equivalent power of 1.3 $nW/H^{1/2}$ were achieved at room temperature under a

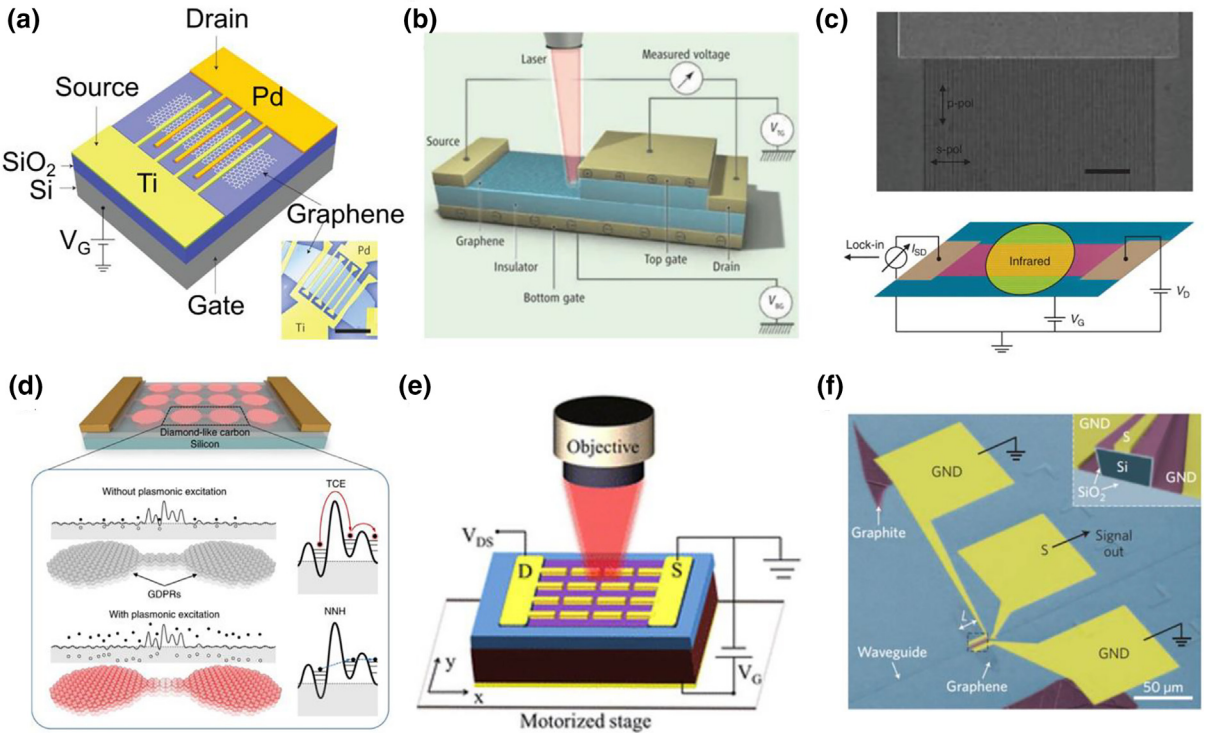

FIGURE 1

Grapehene-based mid-infrared (MIR) photodetectors. (a) Schematic of graphene detector with asymmetric electrodes operating under MIR laser illuminations. (b) Schematic of graphene-based MIR detector operated with the photo-thermoelectric effect. (c) Schematic of the graphene nanoribbon array photodetector with graphene plasmon excitation. (d) MIR detectors based on graphene-disk plasmonic resonators (GDPRs, red circles) connected by quasi-1D graphene nanoribbons (GNRs). (e) Schematic of the antenna-assisted graphene photodetector on a silicon substrate. (f) Micrograph of waveguide-integrated graphene photodetector. Figures reproduced with permission from Ref [21,29,31,32,268,269].

12.2 μm laser illumination. Another way to increase graphene's absorption is to employ metallic nano-antennas to concentrate the light into the graphene layer. The absorption of graphene can be enhanced by metal nanostructures or metasurface on graphene through plasmon resonance [30]. Moreover, the metallic antennas that are commonly designed with gold nanostructures can also serve as efficient carrier collectors. Yao et al. achieved a strong enhancement of the photo-response by 200 times in the MIR antenna-graphene detectors at room temperature as shown in Fig. 1e [31]. Furthermore, the light absorption can also be enhanced by integration with silicon waveguides, where the incident light is concentrated in the waveguide area and absorbed through indirect transition processes as demonstrated by Wang et al (Fig. 1f) [32]. Another advantage of using silicon waveguide is the adjustment of the band alignment, where only holes flow from silicon to graphene is allowed while the electron transport from graphene to silicon is blocked.

Alternative approach is to engineer the band structure in graphene to enhance light absorption in graphene. In graphene photodetectors, the photoresponse is low because of the zero bandgap in graphene, which leads to low light absorption and ultrafast photoexcited carrier recombination rate [33,34]. GNRs with narrow widths have been proposed to overcome these drawbacks because the nanoribbon structure can open a tailorable bandgap in the range of several tens to hundreds of meV due to the quantum confinement effects when reducing the width down to 10 nm [20]. The band structure and the energy gap of pure armchair GNR were calculated using a tight-binding model, indicating that the detectivity could increase with the number of the GNR in a device and with the *n*-doping level, and decreased with the temperature [35]. Ultra-narrow GNR had been fabricated by unzipping single-wall carbon nanotubes to increase the light absorption of the photodetector [36,37] in the visible spectral region. However, the bandgap of graphene nanoribbon achieved through unzipping single-wall carbon nanotubes is relatively large for infrared applications. On the other hand, according to theoretical predictions, GNR with a width of ~10 nm whose band gap is ~0.1 eV could be a proper candidate for MIR photodetector [38–40]. To avoid the carrier scatterings induced by the nano-fabrication processes [41], a high-k capping layer was deposited on the surface of GNR to reduce the Coulomb interactions and scattering loss from defects and GNR edges, thus increasing the photoresponse of the GNR based photodetector [42].

A recent promising and interesting approach is to use twisted bilayer graphene. Small-twist-angle (<2°) bilayer graphene has received extraordinary attention since 2018 due to its exciting physical properties such as superlattice bandgap and substantial modification to the density of states [43,44]. The superlattice bandgap can be optimized by the twist-angle and thus enable tunable photoresponse in the MIR wavelength range [41]. For example, a twisted bilayer graphene (TBG) based device exhibits strong IR responses ranging from 5 to 12 μm, demonstrating extrinsic photoresponsivity of 26 mA W^{-1} at 12.2 μm when

the Fermi level is optimized in 1.81° twist-angle bilayer graphene [34].

Hybrid MIR photodetector

Hybrid photodetector is commonly employed in infrared photodetection where the photo-absorption and carrier transport take place in separate materials. The concept was first proposed for near-infrared photodetectors by Konstantatos et al. in 2012 [17], where strong and tunable light absorption in a quantum-dot layer creates electric charges that are transferred to the graphene transport layer, where they circulate many times due to the high charge mobility of graphene and long trapped-charge lifetimes in the quantum-dot layer. For MIR photodetection, the graphene-based HgCdTe detector technology involves the integration of graphene with HgCdTe photodetectors that combines the best of both materials and allows for higher MWIR detection performance compared with photodetectors using only HgCdTe material. The incorporation of high mobility graphene in this hybrid detector enables a higher responsivity and detectivity compared to conventional MIR detectors. Yu et al. developed a novel type of narrow bandgap oxide nanoparticles, Ti_2O_3 as the light absorber, and achieved high responsivity hybrid Ti_2O_3/graphene photodetector as shown in Fig. 2a. Broadband photoresponse in the MIR regime from 4 μm to 10 μm with high detectivity [45] were achieved in the hybrid device. Alternatively, room temperature photovoltaic response with a cut-off wavelength of 3.4 μm was demonstrated with optimized InAs nanowires with low defect density [13]. The cost-effective and controllable fabrication strategies in this design enable promising applications for flexible and functional hybrid MIR devices. Another design is to use the graphene itself as the broadband light absorber and another graphene layer for carrier transport. Liu et al demonstrated such a hybrid photodetector consisting of two stacked graphene monolayers separated by a thin tunnel barrier. The top graphene absorbs MIR light and generates photoinduced carriers, leading to charges accumulated at the gate. This results in a strong photogating effect on the bottom graphene layer and thus a high responsivity above 1 A/W at 3.2 μm [46].

Substrates also play an important role in graphene photodetection. The photoresponse of graphene on SiO_2 substrate can be significantly enhanced if the surface phonon polaritons of SiO_2 are excited [47,48]. Recently, Gopalan et al. also studied the effect of pyroresistive substrate on graphene photodetection. They placed graphene on a z-cut $LiNbO_3$ platform. The incident light absorbed by the $LiNbO_3$ substrate increases the temperature and, thus, induces polarization (bound) charges at the crystal surface via the pyroelectric effect [49]. The substrates cause doping into graphene, which in turn changes its carrier density and thus the photoconductivity. In addition to certain substrates, photogating also exists in the junctions of graphene-semiconductor heterostructures. For example, Kim et al. reported strong photo-

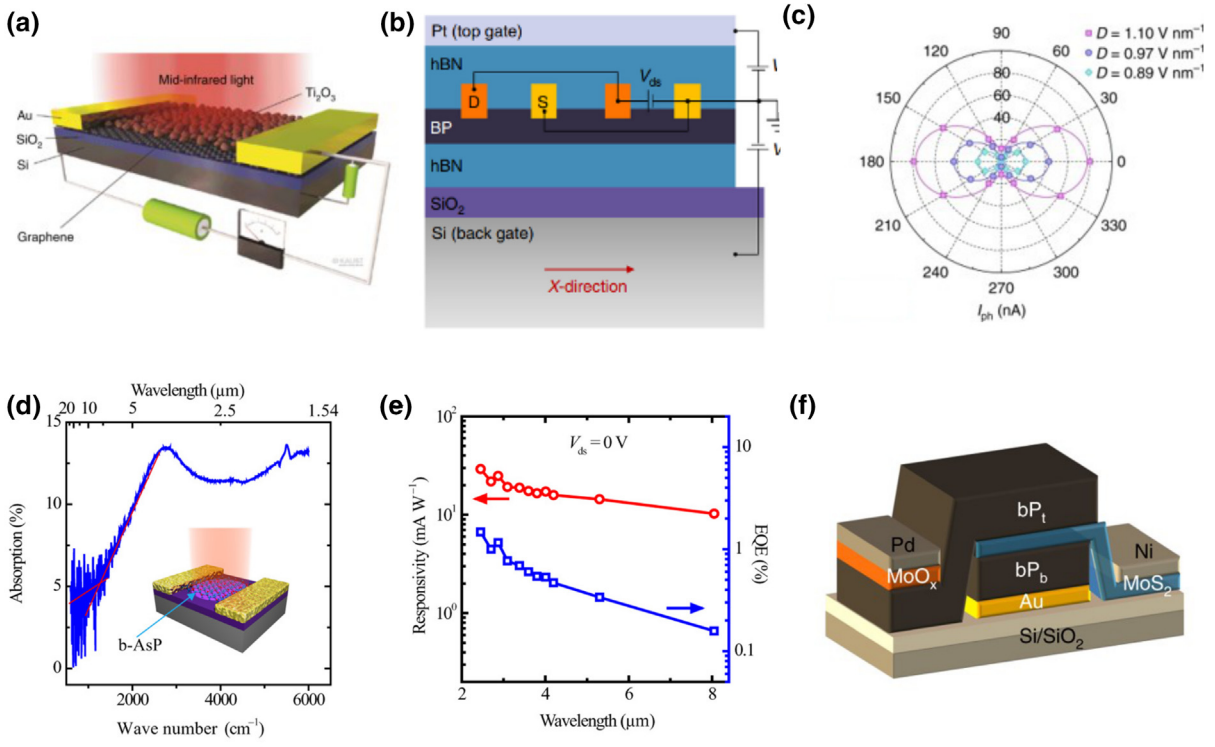

FIGURE 2

Hybrid and other 2D materials-based photodetectors. (a) Schematic diagram of hybrid graphene/Ti_2O_3 nanoparticle MIR photodetector. (b) Structure of the tunable black phosphorene-based MIR photodetector with a dual-gate transistor configuration. (c) Measurement results of the photocurrent at different laser polarization for the 5 μm incident laser. (d) IR absorption and device architecture of 2D b-AsP-based MIR detector. (e) Broadband photoresponse of b-AsP-based detector for wavelength ranging from 2.4 μm to 8.05 μm. (f) Schematic of polarization-resolved bP/MoS2 heterojunction photodiode, showing the heterojunction and contact configuration. Figures reproduced with permission from Ref [45,57,61,63].

gating effects across the tunneling barrier, which enables infrared photodetection with high responsivity at room temperature [50].

MIR detectors with other 2D materials

Recently, BP has been recognized as a promising candidate for MIR photonics due to its moderate bandgap, high carrier mobility and compatibility with a diverse range of substrates [51]. BP and related compounds have already been demonstrated to be a promising MIR candidate due to its unique light absorption and transport properties [52,53]. For example, Tan et al. demonstrated few-layer BP carbide as a broadband light absorber and achieved tunable responsivity and response time at an excitation wavelength above 2 μm [54]. On the other hand, Guo et al. demonstrated black phosphorene MIR photodetector at 3.39 μm with an internal gain up to 10^5 and external responsivity of 82 A/W [55]. Because the intrinsic bandgap of BP is larger than 0.33 eV, the operational wavelength range is limited to be below 3.7 μm [56]. Nevertheless, Chen et al. reported a widely tunable BP MIR photodetector with a vertical electrical field modulation as shown in 2b and c, which showed a polarization-sensitive photoresponse from 3.7 μm to beyond 7.7 μm thanks to the Stark effect [57]. The high photoresponse at MIR wavelengths and the large dynamic bandwidth, together with its unique polarization-dependent response induced by the asymmetric crystal structure, make BP an interesting and promising material for mid-infrared detection [58,59]. Another strategy to extend the operation wavelength range is by doping the phosphorus to form phosphorus alloys. Arsenic doped BP sandwiched within hexagonal boron nitride was demonstrated as broadband, stable MIR photodetector exhibiting remarkable photoresponsivity originated from the intrinsic photoconductive effect [60]. In the meantime, black arsenic phosphrous (b-AsP) was reported as an efficient long-wavelength IR detectors with stable, room temperature operation up to 8.2 μm as shown in 2d and e [61]. A MIR spectrometer in the 2–9 μm spectral range, utilizing a single tunable black phosphorus photodetector along with a unique spectral learning procedure was reported as an on-chip spectrometer with compact footprints [62]. The as-designed single-detector spectrometer showed remarkable potential in the reconstruction of the spectra of both monochromatic and broadband light in the MIR regime. On the other hand, BP/MOS_2 heterojunction photodiodes were explored as MIR photodetectors as shown in Fig. 2f. The performance was enhanced by optimizing the device structure. For example, polarization-resolved detection with detectivity as 1.1×10^{10} cm $Hz^{½}$ W^{-1} was achieved [63]. Another element 2D semiconductor, telluene, was reported as a promising candidate for MIR light detection due to the small bandgap, stability, and low-cost solution synthesis method [64]. Amani et al. [65] demonstrated multilayer tellurene with an indirect bandgap of ~0.31 eV as a high-performance MIR photodetector integrated with optical cavity substrates. Furthermore, FET-based tellurene MIR photodetectors with high gain and large bandwidth were obtained through the photogating effect [66], indicating that tellurene could be a good candidate for polarization-sensitive and ultrafast MIR detectors [67–69].

In addition, MIR photodetectors based on reduced graphene oxide, which has lower carrier mobility but tunable bandgap compared with graphene, have also been demonstrated. Trung et al. demonstrated a reduced graphene oxide FET which exhibited a high response under MIR light illumination [70]. However, the formation of a thin, large, continuous reduced graphene oxide network remains a challenge. Hydrophobic copolymer (P(VDF-TrFE)) has been employed as a matrix for reduced graphene oxide to obtain high IR responsivity, reproducibility and stability [71]. Similar to GNRs, graphene oxide nanoribbons with proper widths were also demonstrated as infrared photodetectors with high selectivity, high sensitivity, and high response speed [72]. Recently, Yu et al. demonstrated that 2D atomically thin $PtSe_2$ exhibits a tunable bandgap in the MIR via layer and defect engineering and broadband photodetection with a photoresponsivity of 4.5 A/W and a detectivity of 7×10^8 Jones [73].

Furthermore, several other 2D materials have been discovered as a new topological phase of matter, named Weyl semimetal. Their surface features a non-closed Fermi surface and the electrons in the 2D materials behave as Weyl fermions [74–77]. Theoretical work has predicted that Weyl semimetals, such as $MoTe_2$, WTe_2, etc., could be good candidates for high-sensitive and broadband infrared photodetector [78]. Due to the combination of inversion symmetry breaking, chirality anomaly and finite tilts of the Weyl spectra [79], these Weyl semimetals feature an interesting chirality selectivity for MIR photodetection [78,80]. Recently, Wei et al demonstrated MIR polarization sensitive photodetector by tuning the orientation of nano-antennas on the surface of semimetals [81]. The typical performance of the recent 2D material-based IR photodetectors are listed in Table 1.

Optical modulator

Modulation of MIR radiation is important in many applications. High-speed amplitude/phase modulation are essential for amplitude-modulated/phase-modulated spectroscopy and sensing [82,83]. Large modulation depth, large bandwidth and fast modulation speed are desirable for applications such as MIR free-space communication [84,85]. The dimension of the modulators is crucial for realizing compact optoelectronic devices and the spatial resolution for MIR spatial light modulators (SLM) and single-pixel imaging [84,86,87].

Amplitude modulator

Amplitude modulator depends on the tunable light absorption by the active materials used in the amplitude modulators. Although the absolute absorption of graphene in the MIR regime is weak, nano/microstructures can be incorporated to enhance the interaction between the graphene and MIR light. A number of related works have been reported in the literature [88–93]. The patterned graphene also can be directly coupled with either free-space light or evanescent wave in the waveguide. It is theoretically shown that the control of the graphene leads to tunable passband/stopband of the waveguide and thus the modulation of MIR light [94–98]. The performance of 2D-material-based modulators (such as modulation depth, tuning range, and response time) can be improved by integrating graphene with plasmonic nano-antenna [99,100]. Yao et al. designed a tunable MIR modulator comprised of a doubly resonant antenna array on top of large-area graphene (Fig. 3a). At the wavelength of 7.8 μm, the intensity modulation can reach a maximum of 30% with tunable

TABLE 1

Performance of 2D materials-based IR photodetectors. (LIR: Long-wave infrared; SWIR: Short-wave infrared).

System	2D Materials	Detection range	Responsivity (A W^{-1})	Response time (s)	Detectivity (Jones)	References
Elemental 2D materials	Graphene	Vis-MIR	8.6	>10	–	[270]
	BP	MIR	82	10^{-4}	$\sim 1.2 \times 10^{8}$	[43]
	Te	MIR	13	0.57	2×10^{9}	[65]
Compound 2D materials	Bi_2Se_3	SIR	23.89	0.54	8.0×10^{10}	[271]
	Black-AsP	MIR-LIR	15	0.54×10^{-3}	4.9×10^{9}	[61]
	$MoTe_2$	SWIR	10^{-2}	10^{-3}	1.3×10^{9}	[272]
	$PtSe_2$	Vis-MIR	4.5	10^{-3}	7×10^{8}	[73]
	WTe_2	MIR	3.6×10^{7}	–	–	[273]
Hybrid structures	Graphene/Ti_2O_3	MIR	>120	10^{-3}	2×10^{8}	[45]
	Graphene/MoS_2	SWIR	10	0.28	–	[274]
	Graphene/BP	SWIR	3.3×10^{3}	4×10^{-3}	–	[275]
	MoS_2/BP	MIR	153.4×10^{-3}	1.5×10^{-5}	2.13×10^{9}	[276]
	MoS_2/BP	SWIR	0.9	4×10^{-6}	1.1×10^{10}	[63]
	MoS_2/PbS QD	SWIR	10^{7}	17	5.5×10^{15}	[277]

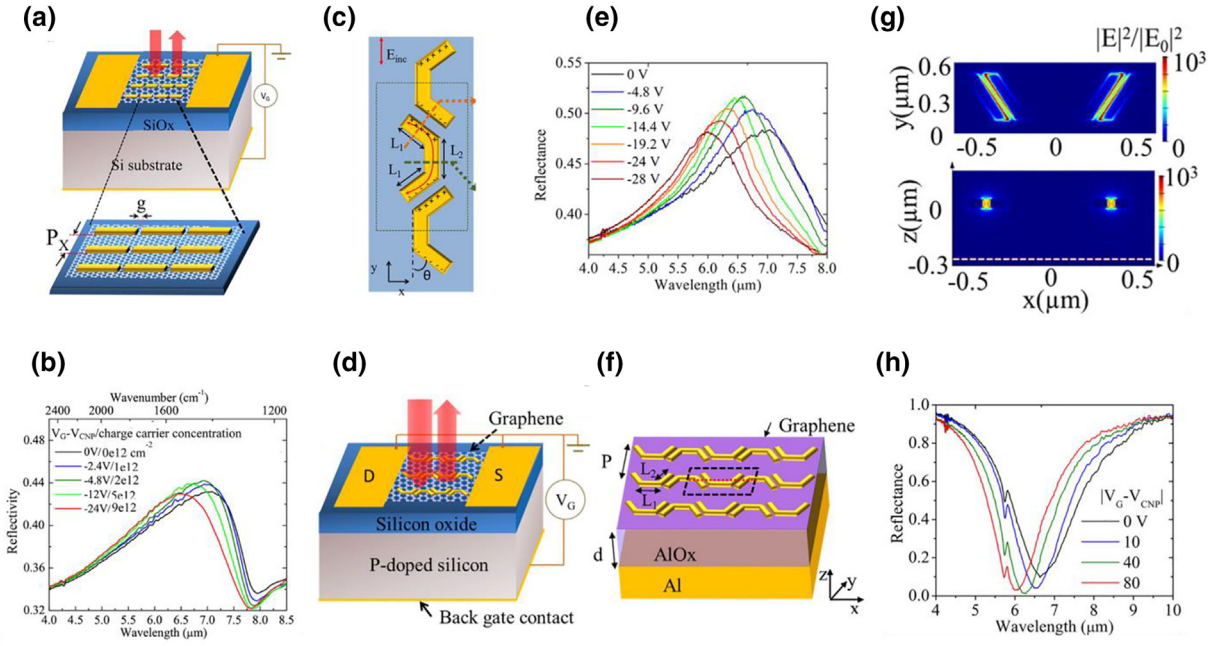

FIGURE 3

(a) Schematic of a double resonant plasmonic device with back gate voltage control and the antenna array on the graphene. (b) Measured reflectivity spectra after the chemical doping under different gate voltages for device in (a). (c) Top view of a laterally coupled antenna design with a bending angle θ at both ends of the antenna. (d) Schematic structure with optimized antenna design. (e) Measured reflectivity spectra under different gate voltages for device in (d). The tuning range and modulation depth are improved compared with the results in (b). (f) Schematic of the graphene metasurface device with a back mirror, which also functions as a back gate for graphene. (g) Simulation of electric field in horizontal (top) and vertical plane (bottom). (h) Measured reflectivity spectra under different gate voltages for device in (f). The modulation depth can be 95%. Figures reproduced with permission. (a), (b) Ref. [100]; (c)–(e) Ref. [101], (f)–(h) Ref. [85].

resonance wavelength over 650 nm, as shown in Fig. 3b. To further increase the spectral tuning range and the modulation depth, Yao et al. optimized the antenna, a typical antenna design of which is shown in Fig. 3c [101]. The parallel antennas are shifted with each other such that the bottom of one antenna interacts with the other one on the top. The coupling can be further enhanced with optimized antenna designs. By utilizing the metal–insulator-metal plasmonic mode, the effective mode index becomes more sensitive to the carrier concentration of the graphene. A schematic diagram of the device and measurement setup is shown in Fig. 3d. A modulation depth of 70% is achieved at a wavelength of 7 μm and the tuning range of the resonance wavelength is 1100 nm, as shown in Fig. 3e. However, due to the RC limitation, the 3 dB cut-off frequency is limited to about 30 MHz.

In the meanwhile, several theoretical works explored the possibility of optical modulation with graphene by using metamaterial structures based on Fano resonance [102,103]. Aygar et al. demonstrated that tunable graphene fractal metamaterials with both top and back gating schemes can achieve a spectral tuning of 8% of the resonance wavelength [104]. Dabidian et al. [105] and Yao et al. [85] also successfully demonstrated the integration

of graphene with metamaterials for the MIR optical modulation. Combined with the electrostatic doping of the graphene, the measured reflectivity at the resonance can be modulated by up to 90%. Yao et al. demonstrated a high-speed tunable perfect absorber with an optical modulation depth up to 95% [85]. The device configuration is shown in Fig. 3f. An optimized metamaterial array is fabricated on top of a dielectric layer which is placed on a bottom metallic layer. The graphene is placed in between the metasurface and the dielectric layer. A strong electric field enhancement is obtained in the gap of the structure as suggested by the simulation (Fig. 3g). Through carefully engineering the conductivity of the metasurface, the critical condition can be achieved such that 100% absorption can be reached. The measured reflection spectra of this device are shown in Fig. 3h. As the gate voltage is tuned away from the charge neutral point, the increased carrier density in the graphene blue shifts the resonance of the metasurface. A perfect absorption occurs at 6.3 μm when the gate voltage is increased up to 40 V. In addition, the response time of the device is measured to be 10 ns, limited by the speed of the mercury cadmium telluride (MCT) detector. The calculated 3-dB cut-off frequency is as high as 20 GHz, calculated based on the circuit model as proposed by Li et al. [100]. In these works, a strong intensity modulation can be realized by incorporating metamaterials with graphene. Such a high-speed device also has great promise for applications in imaging, communication, and optical switching, etc.

Recently, the investigation of other 2D materials for the MIR optical modulation has sparked a myriad of research activities, among which the study of BP has shown a variety of attractive results. As the bandgap of BP varies from 0.3 eV to 2 eV with the decreasing number of layers [106], this bandgap range is applicable for the MIR modulation. The optical response of multilayer BP was studied in detail by Lin et al. [107]. The band diagram of BP with a thickness of 5–6 nm is shown in Fig. 4a. For the intrinsic case, the corresponding carrier density is 1.4×10^{10} cm^{-2} and the corresponding bandgap is about 0.62 eV. With the applied bias, the quantum confined Franz-Keldysh (QCFK) effect dominates, and the bandgap is reduced due to the increase of carrier density. Simultaneously, the Fermi level E_f moved into the conduction band and further increase of the positive bias blocks the optical transition, as described by the Pauli-blocked Burstein-Moss shift (BMS). As the BMS is dominating over QCFK, the net result is a broadening of bandgap at the high positive bias level, as shown in Fig. 4b. Such a mechanism can be applied for the MIR optical modulation. As a proof-of-concept, a simple waveguide-integrated BP modulator is studied with a similar structure to the work by Liu et al. [108] as shown in Fig. 4c. The transverse-magnetic (TM) mode is selected to enhance the interaction between the propagating light and BP. The results in Fig. 4d show that with a 6-nm thick BP at 2.1 μm wavelength, and a 20-nm thick BP at 3.3 μm wavelength, the propagation loss can be tuned at 0.5 dB/μm and 0.6 dB/μm, respectively. The figure-of-merit (FOM), defined as the ratio of extinction ratio over the insertion loss here, exceeds that of the conventional SiGe-based modulators [109]. Whitney et al. experimentally demonstrated the tunable optical response of BP as shown in Fig. 5a, which is the first experimental report of the optical modulation with BP in the MIR region. Fig. 5b shows the transmission extinction as a function of photon energy for the device with a 6.5 nm thick BP at 80 K temperature, under different gating voltages [110]. The features in the spectrum were interband transitions between different conduction and valence bands (Fig. 5c). The sample is initially heavily hole-doped, whose Fermi level locates about 50 meV below the valence band. Therefore, within the measurement spectral range, optical transitions mainly occur between the second lowest state in the conduction band (c2) and the second highest state in the valence band (v2), corresponding to an absorption peak between 0.5–0.7 eV. This situation is also depicted by the black curve in Fig. 5d. When a sufficiently high negative bias is applied, the Fermi level moves up into the bandgap, enabling the c1-v1 transition, which accounts for the absorption peak around 0.45 eV (see the blue curves in Fig. 5b and d). In contrast, if a positive gating is applied, the Fermi level gradually goes down and starts to block the c2-v2 transition if it is located blow v2 state (red curve in Fig. 5d). Therefore, the curves corresponding to the positive biases in Fig. 5b feature an absorption dip between 0.5–0.7 eV. Therefore, the spectra are decided by the combined QCFK and BMS effect as studied in previous reports [107]. Fig. 5e shows the measurement result for a 14 nm thick BP sample. In this case, more energy states are involved as the bandgap becomes narrower. Without bias, the BP is n-type with a Fermi level lying in the bandgap. Under negative bias, the Fermi level gradually moves into the conduction band and blocks some interband transitions, leading to a decreasing absorption for an increasing negative bias. It demonstrates that broadband tunable transmission can be achieved with multilayer BP, which may be promising for future optoelectronic applications in the MIR region.

Other than graphene and black phosphorus, the pursuit of other materials for modulating the intensity of MIR radiation is still ongoing. For instance, tuning the gating voltage of few-layer $MoSe_2$ flakes can modulate the transmission of near-infrared to MIR light by ~10% [111]. In this work, the authors employed an electric-double-layer gating technique with ionic liquid to increase the modulation depth. Researchers also proposed that tellurene could be used to modulate the transmission of a MIR waveguide. The Pockels effect in tellurene could be harnessed to build a Mach-Zehnder interferometer [112]. It was estimated that half-wave voltage length product of a 40 nm tellurene is approximately 4.7 Vcm, which is 10 times better than the state-of-the-art EO modulators in the MIR region.

Phase modulator

Phase is another fundamental property of light. The ability to control the phase provides greater flexibility in changing the wavefront, which has important applications in hologram, beam steering, frequency modulation, etc. The majority of the 2D material modulators are based on the shifting of the resonant position in the transmission or reflection spectrum upon gating. Not only will this resonance sweeping lead to amplitude modulation, but it would also induce phase modulation since the phase of the oscillation varies rapidly across a resonance. However, experimental investigations of such phase modulation are rare despite some recent theoretical proposals [85,99,105]. The main challenge of constructing a phase modulator in this way

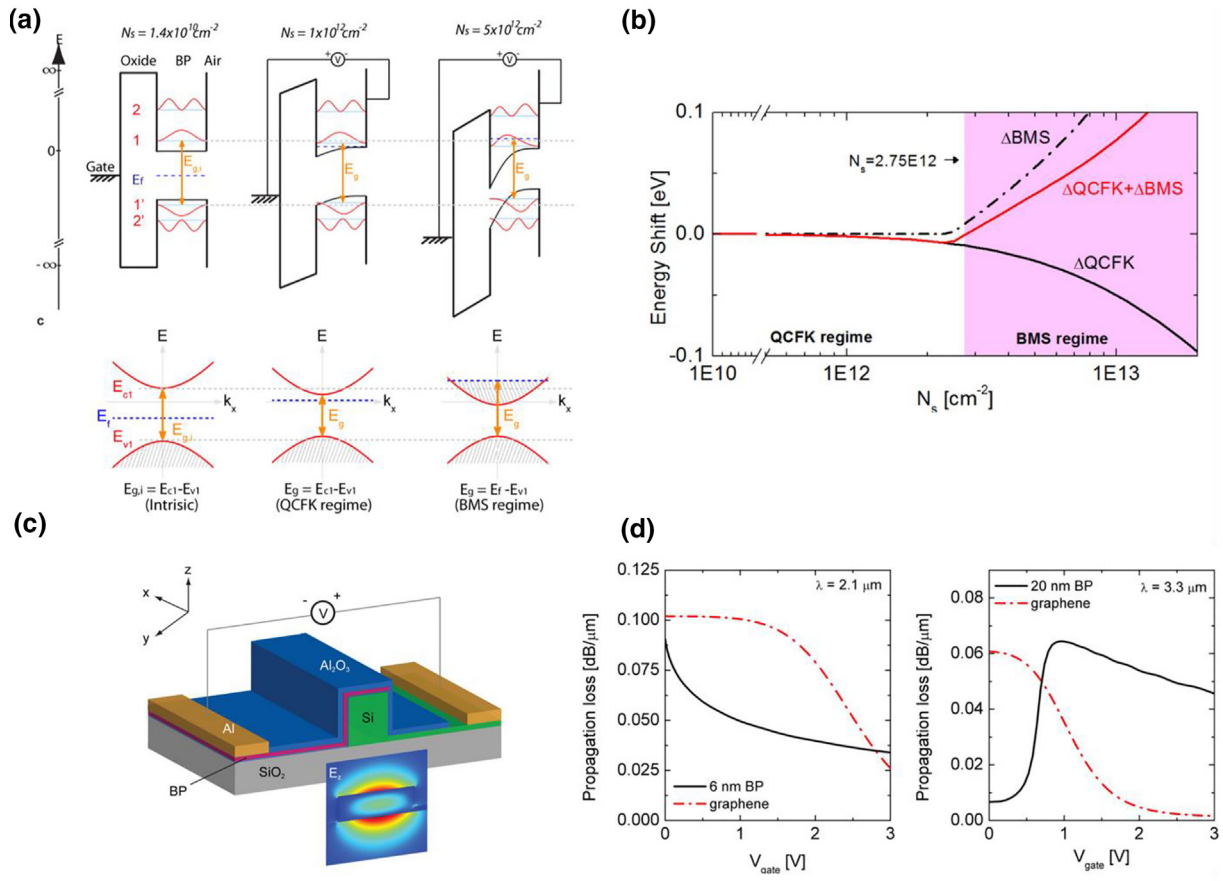

FIGURE 4

(a) Energy band diagram of multilayer BP under different carrier densities. (b) The energy shift of bandgap of multilayer BP under different carrier densities. (c) Schematic of a waveguide-integrated multilayer BP modulator. (d) Comparison of propagation loss between waveguide-integrated multilayer BP and single-layer graphene modulator. Figures reproduced with permission from Ref. [107].

is how to maintain the amplitude while modulating the phase [113].

Recently, Dabidian et al integrated single-layer graphene with Fano-resonant plasmonic metasurface (Fig. 6a) which is supposed to sharpen the resonant peak so that the phase changes is more sensitive to small resonance shift [83]. Experimental results indicated that the phase of the reflected MIR light can be tuned by 55° via electrostatic gating (Fig. 6b). The according amplitude change is shown in Fig. 6c, where the phase modulation region corresponding to 10% variation of the reflectivity is shaded. Sherrott et al used gold nanoresonators on graphene with gold back mirrors to realize a MIR phase modulator as shown in Fig. 6d [114]. Phase modulation at wavelengths of 8.2 μm, 8.5 μm, and 8.7 μm is shown in Fig. 6e. A smooth modulation of phase with applied voltage from 0° to 206° at a wavelength of 8.7 μm can be observed. The main limitation of the device is still the high optical loss and the large intensity modulation as shown in Fig. 6f. A summary of the 2D material-based MIR modulators is given in Table 2.

Plasmon and phonon polaritons

Surface plasmon polaritons (SPPs), resulted from the coupling between the optical field and the collective oscillations of the free carriers at the conductor–dielectric interface, have been an active research topic in the past two decades. The most interesting property of SPPs is their capability of confining and controlling light in the subwavelength scale, enabling strong light-matter interaction and flexible wavefront/beam engineering. The SPP is excited when the permittivity of a material has a negative value to the permittivity of its dielectric environment. The plasmonic contribution of a material's permittivity depends on the doping concentration and effective mass of the charge carriers. The noble metal-based SPPs in the MIR have week confinement. This problem can be addressed by structuring the metal surface or by using highly doped semiconductors, which has smaller free electron concentration around 10^{18}–10^{19} cm^{-3} [115–117]. The recent studies on phonon polaritons (PhPs) provide an alternative way to achieve high spatial confinement. The phonon polaritons also feature in low material loss as the lifetime of phonon is at least one order longer than the typical lifetime of the plasmon counterpart at similar wavelengths.

Graphene plasmonics

Graphene plasmonics simultaneously exhibit high confinement and tunability. The dispersion of graphene plasmon is approximately given [118]

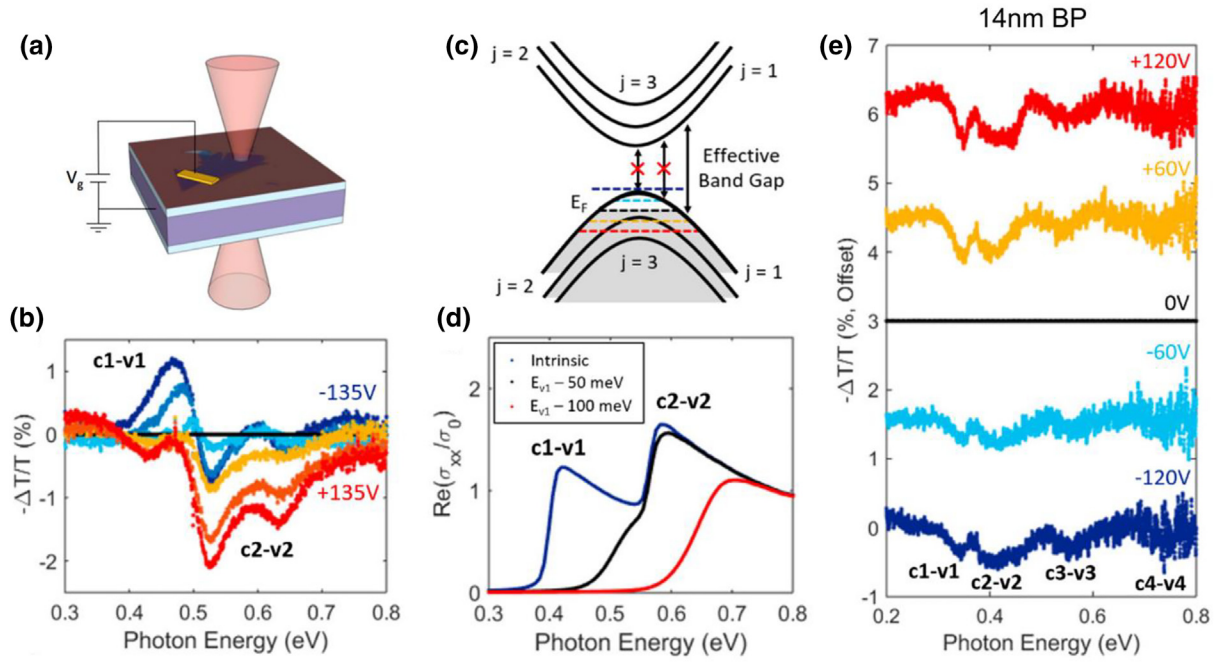

FIGURE 5

(a) Schematic illustration of the MIR Black Phosphene (BP) modulator. (b) Fourier Transform Infrared Spectrometry (FTIR) transmission extinction of a 6.5 nm thick BP flake versus photon energy normalized to zero bias under various gating voltages. (c) Schematic of electronic band structure and allowed interband transitions at different voltages (Fermi levels). (d) Calculated optical conductivity of a 6.5 nm thick BP flake at different Fermi levels, normalized to the universal conductivity of graphene. (e) FTIR transmission extinction of a 14 nm thick BP flake versus photon energy normalized to zero bias. Figures reproduced with permission from Ref. [110].

$$\omega = \sqrt{\frac{e^2 E_F q}{2\pi \hbar^2 \varepsilon_0 \varepsilon_r}}$$

where q is the wavevector of the graphene plasmon mode, ω is the angular frequency, $\varepsilon_r = (\varepsilon_1 + \varepsilon_2)/2$ with ε_1 and ε_2 being the dielectric constants of the dielectrics that sandwich the graphene sheet. A small change in graphene's carrier concentration shifts its Fermi level significantly due to its linear electronic bandstructure and a change in Fermi level directly tunes the optical response of graphene.

The graphene SPP wavelength λ_{sp} is found to be related to free-space wavelength λ_0 as [119]

$$\frac{\lambda_{sp}}{\lambda_0} \approx \frac{2\alpha}{\varepsilon_r} \frac{E_F}{\hbar\omega} \propto \sqrt{n}$$

where $\alpha = e^2/\hbar c = 1/137$ is the fine-structure constant. If the carrier concentration is controlled by electrostatic gating, then $n \propto v_g$. Therefore, the SPP has a $\lambda_{sp} \propto \sqrt{V_g}$ dependence, as observed experimentally in previous literatures [120–122]. In the MIR region, $E_f/\hbar\omega$ can be tuned to be close to 1. Therefore, λ_{sp} can be two orders of magnitude smaller than λ_0 in MIR, implying an ultra-strong mode confinement. In 2012, Chen et al. [28] and Fei et al. [120] visualized the propagating and localized graphene SPPs in real space. They launched the graphene SPPs by illuminating the sharp tip of an atomic force microscope (AFM) with a focused MIR beam (Fig. 7a). The backscattered radiation is recorded simultaneously with the topography, yielding nanoscale resolved near-field images in the MIR wavelengths (Fig. 7b–d). The tip-excited surface wave propagates along with the graphene and is then reflected by the graphene boundaries, the two counter-propagating waves interfere to produce the interference fringes in the near-field images. The plasmon wavelength λ_{sp} can be extracted by measuring the fringe distance, which is ~130 nm, indicating a plasmon wavelength of ~260 nm for λ_0 = 9.7 μm and E_f = 0.4 eV, and λ_0/λ_{sp} = ~40. The authors demonstrated in situ tunable behavior of the graphene plasmons by varying the gate voltage (Fig. 7d and e). When the Fermi level is near the Dirac point, the strong plasmon damping via interband optical transition quenches off the plasmons. As the Fermi level is pushed away ($|E_F| > E_p$), these transitions are forbidden and the plasmons are switched on.

To launch the plasmon of graphene, one must compensate the in-plane wavevector of the incident light to match the plasmon wavevector that is often tens of times larger. In the above case, this is done by using an AFM tip, which provides the necessary momentum compensation. An alternative approach is to pattern graphene into nanostructures to excite plasmon in the MIR region as demonstrated by Fang et al. [90], where the plasmon can be resonantly excited without the assist of any additional coupler. The plasmon energy scales with Fermi level according to Eq. (2), $\lambda_{sp} = \lambda_0/n_{eff} \propto E_f$ indicating that the effective refractive index of graphene decreases with the Fermi level. Therefore, the effective optical size of the nanodisk shrinks as the Fermi level increases, leading to a blue shift of the resonant peak. The increasing extinction peak with the Fermi level can be understood from two aspects: (1), the increased Fermi level produces more carriers to interact with the incident light, leading to a stronger plasmon strength; (2) as $\lambda_{sp} = \lambda_0/n_{eff} \propto E_f$, the increased plasmon wavelength reduces the momentum mismatch between the free space and the plasmon modes, resulting

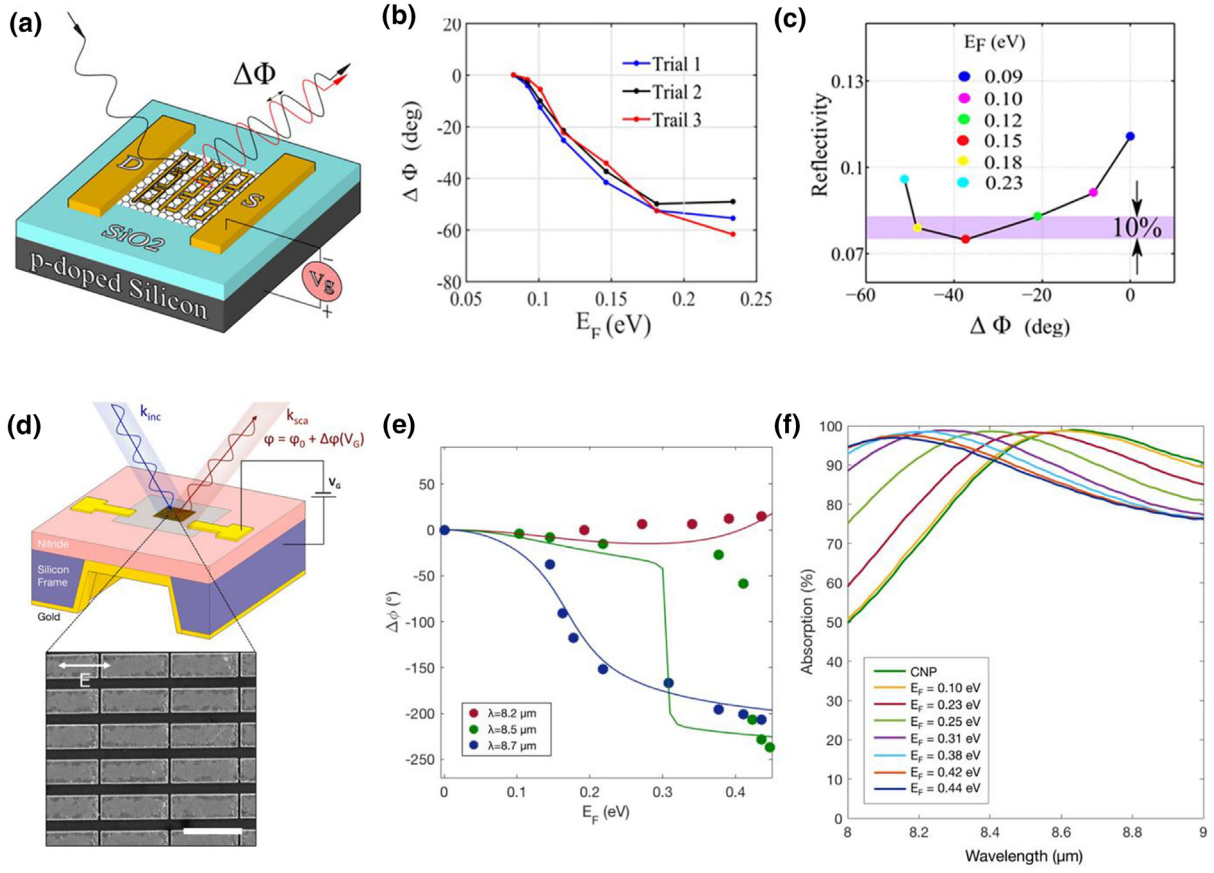

FIGURE 6

(a) Schematic for graphene-induced phase modulation of the reflected MIR wave (b) Measured hase change ΔΦ as a function of the Fermi energy for three independent experiments (Trials 1–3). (c) Reflectivity-phase diagram using the data from the Trial 1 as a function of color-coded Fermi energy. All measurements are performed at λ_0 = 7.69 μm. (d) Schematic of a gate-tunable device with a gold mirror for control of reflected phase. The inset shows an SEM image of gold resonators on graphene, where the white scale bar indicates 1 μm. (e) Phase modulation at wavelengths of 8.2 μm, 8.50 μm, and 8.7 μm (circles experiment, line simulation). (f) Absorption spectra measured in FTIR at different gate voltages corresponding to indicated Fermi energies. Figures reproduced with permission: (a)–(c) Ref. [83]; (d)–(f) Ref. [114].

TABLE 2

Summary of 2D material-based optical modulators in the MIR wavelength region.

Wavelength (μm)	Material	Type	Modulation depth	Gating method/Speed	Remarks and year	Ref.
4.5/6.2	Graphene	Amplitude/ Transmission	~10%	Silicon back gate	With metallic antenna or graphene nanoresonator, 2012–2013	[88,92]
2.4/7.3	Graphene	Amplitude/ Reflection	15% – 30%	Ionic liquid/gel	With Fano resonant plasmonic nanostructures or graphene disk, 2014	[89,91]
7–8	Graphene	Amplitude/ Reflection	30% – 90%	Silicon back gate	With plasmonic resonators, 2013–2015	[100,101,105]
6	Graphene	Amplitude/ Reflection	95%	Metal back gate	With metallic antennas + back mirror, high speed (up to 20 GHz), 2014	[85]
2.1/3.3	Multilayer black phosphorus	Amplitude/ Waveguide-based	0.5–0.6 dB/ μm	Silicon back gate	Waveguide-based device, 2016	[107]
2.5	Multilayer black phosphorus	Amplitude/ Transmission	15%	Silicon back gate	Without any resonant structure, 2017	[110]
7.7	Graphene	phase/Reflection	55°	Silicon back gate	With Fano resonant plasmonic nanostructures, 2016	[83]
8.7	Graphene	Phase/Reflection	206°	Metal back gate	With metallic antennas + back mirror, 2017	[114]

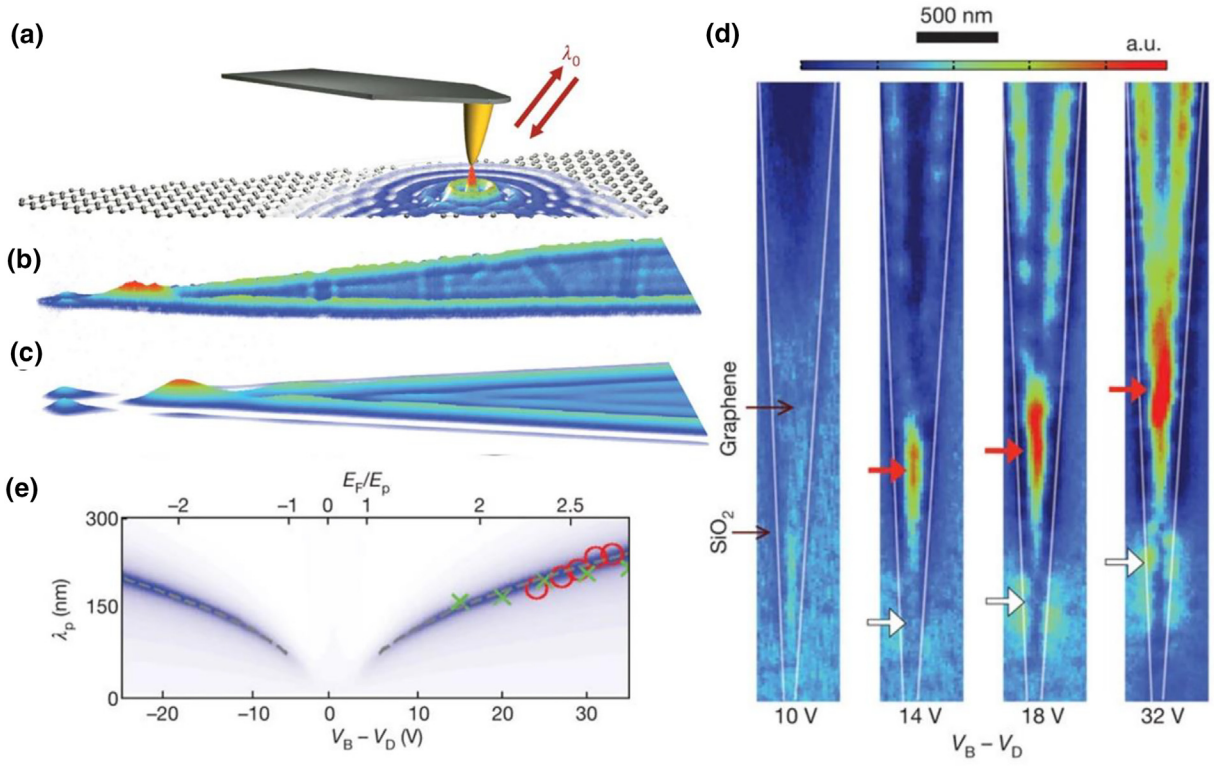

FIGURE 7

(a) Shematic of the excitation and measurement of the graphene plasmons using an atomic force microscope (AFM) tip and a focused MIR beam. (b). Near-field amplitude image of the graphene plasmon on a tapered graphene ribbon on a 6H-SiC substrate, the excitation wavelength is 9.7 μm. (c). Calculated local density of optical states (LDOS) at a distance of 60 nm from the graphene surface. (d) Near-field amplitude images of the graphene plasmons under various gating voltages, showing active control of the plasmon behavious. At 10 V, the graphene plasmon is switched off due to the high onset of interband optical transition as the Fermi level approaching the Dirac Point. Increasing the gate voltage tune the plasmon to longer wavelength, making the localized modes (indicated by the white and red arrows) shift upward. The excitation wavelength in these measurements is 11.06 μm. (e) Graphene plasmon wavelength as a function of the gate voltage. The red circules and green markers are the experimental data while the colour map corresopnds to the calculated reflection coefficient. Figures reproduced with permission from Ref. [28].

in strong coupling of the incident light to the plasmon modes [92]. In this case, the hybridization occurs between the disk and hole plasmon modes in graphene nanorings, which splits the energy level into two well-separated ones. The plasmon frequency of the anti-bonding mode can thus be pushed to 0.34 eV (λ_{sp} = 3.7 μm) for a nanoring structure with 60 nm inner diameter and 100 nm outer diameter.

Similarly, Brar et al. demonstrated plasmonic mode in graphene nanoribbons (Fig. 8a and b) [92]. The graphene nanoribbon structure serves as plasmonic nano-resonators that support highly confined optical mode, as shown in Fig. 8c. For $E_F = -0.22$ eV, λ_0/λ_{sp} is equal to 49 in 50-nm wide nano-resonators. This ultra-tight confinement of the optical modes is highly desirable for strong light-matter interactions. For some quantum phenomena (e.g., Purcell effect), Q/V_{eff}, with Q being the Q factor and V_{eff} the mode volume, is a figure of merit. It was estimated that the value of Q/V_{eff} for the graphene plasmon mode here is in the range of 10^6–10^7 λ_0^{-3} , which is two orders of magnitude larger than what has been achieved using the plasmon modes of metal nanostructures [123,124]. The dependence of the optical transmission spectra on the width of the nanoribbon and Fermi level are represented in Fig. 8d and e, respectively.

When two monolayer graphene are stacked together with a small twisted angle, a Moiré pattern can be formed which modulates the local electronic and photonic properties at the nanoscale, as shown in Fig. 9a [125,126]. The grain boundary of monolayer graphene has been proved to be an efficient scatterer of graphene plasmon [127]. The domain walls (solitons) of plasmonic photonic crystal created using twisted bilayer graphene (TBG) are also efficient scatters of graphene plasmon because the topologically protected chiral 1D states increase local optical conductivity. The experimental results proved the scattering of polaritons in the TBG forms a polaritonic crystal, whose calculated bandstructure is shown in Fig. 9b. Although the reported TBG-based polaritonic crystals have a negligible bandgap, the authors predict that a complete plasmonic bandgap can be opened with higher scattering strength at solitons (as shown in Fig. 9c). This work realizes a nano-light photonic crystal without any top-down fabrication process and laid a foundation for exploiting the plasmonic properties of graphene in the quantum regime. Fig. 9d and e show the real-space mapping of Moiré pattern for a TBG under different gating voltage at different frequencies. Fig. 9f and g are the calculated magnitude and phase of the corresponding near-field signal, which agrees well with the

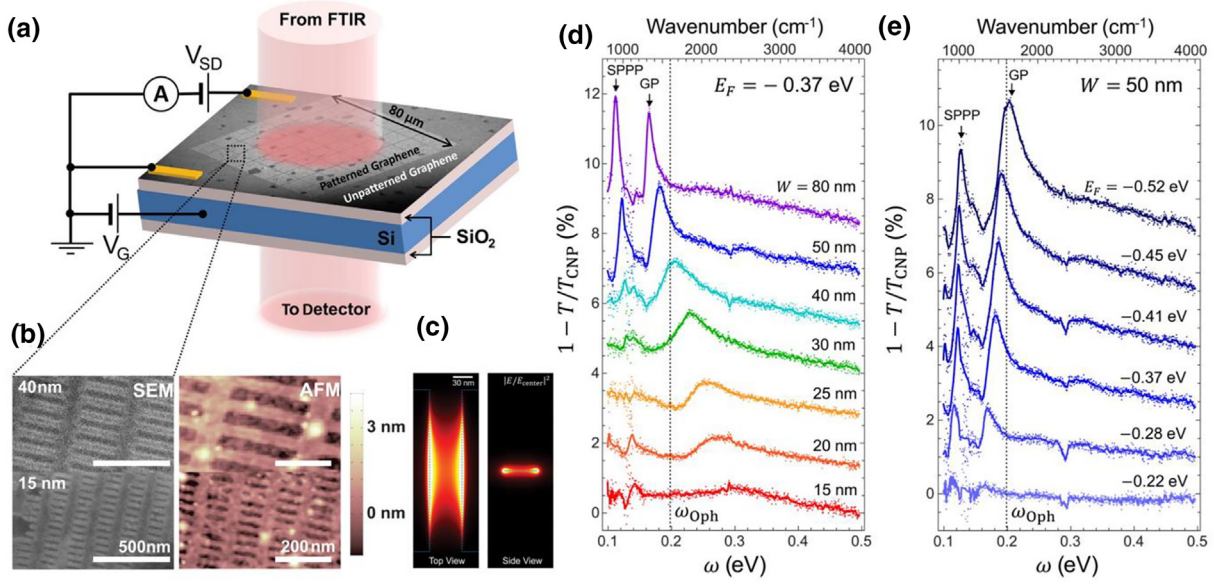

FIGURE 8

(a) Schematic of the device with graphene nanoribbons in a back gate configuration. The graphene sheet was grounded through Au/Cr electrodes that can also be used as the source-drain contact for graphene sheet conductivity measurements. (b) SEM and AFM images of 40 and 15 nm graphene nanoribbon arrays. (c) Calculated light intensity distribution of the graphene plasmonic mode in a 50 nm wide graphene nanoresonator with $E_F = -0.37$ eV. (d) Width dependence of optical transmission of the device with $E_F = -0.37$ eV. (e). Fermi level dependent optical transmission of the device. Figures reproduced with permission from Ref. [92].

measurement results. Recently, h-BN flakes are stacked with small twisted angles and the release of strains forms similar superlattice patterns consisting of line defects and hexagonal domains of AA′ stacking [128]. The twisted bilayer of α-MoO_3 has attracted much attention in recent years. The iso-frequency contour of the hybridized polariton wave could be tuned from elliptic to hyperbolic by tuning the twisted angles and it holds promise in compact photonic circuitry [129–132]. Twisted bilayer of 2D materials provides a new experimental platform for Moiré system and condense matter physics [133].

The strong light confinement of graphene plasmon is very promising for enhanced light-mater interactions in the MIR region. After several theoretical proposals [134,135], Li et al. demonstrated graphene-plasmon-enhanced vibrational sensing of surface-adsorbed polymers at ~6 μm wavelength using graphene nanoribbons [136], They verified that the decay length of the surface plasmon evanescent wave is ~10 nm. The signal of the C=O vibrational mode can be enhanced by several times. In this work, frequency tuning is achieved by optimizing the width of the nanoribbons. For example, Rodrigo et al. exploited the unique tunable graphene plasmon to demonstrate an unprecedented high-sensitivity graphene biosensor for chemically specific label-free detection of protein monolayers as shown in Fig. 10a [137]. Graphene was patterned into nanoribbons which are electrically interconnected. The amount of the protein was determined by measuring the spectral shift ($\Delta\omega$) of the plasmon resonance induced by the presence of the protein, while the detailed structural information can be inferred from the narrow dips in the extinction spectra (such as the dips in the spectra labeled V_2 and V_3 in Fig. 10b). In operation, the Fermi level of the graphene is tuned dynamically to move the broad plasmon resonance peak to match the vibrational bands of the target proteins. Fig. 10c and d present an example of such measurements for recombined protein A/G and IgG. Fig. 10e compares the extinction spectra of the two devices before and after protein immobilization when the plasmon resonance is away from the vibrational resonances of the protein. The redshift of the resonance for the graphene is about 160 cm^{-1}, which is ~6 times the value obtained by the common gold antenna (27 cm^{-1}). Graphene biosensor has much stronger surface-enhanced IR absorption (SEIRA) signal than the Au-based plasmonic biosensors as shown in Fig. 10f. These results demonstrated the advantages of graphene biosensors in both refractive index sensitivity and SEIRA sensitivity, indicating their capability of sensing over a broad spectrum with a single device.

Apart from sensing, graphene plasmon also finds applications in near-field imaging [138], and the waveguiding nature of the graphene SPP inspires its use as a new platform for integrated photonic circuits [139]. For example, it can be used to enhance the evanescent information of the MIR near-field microscopy [138].

Plasmon and phonon polariton in graphene heterostructures and other 2D materials

Other than graphene, plasmon in other 2D materials have also been explored in the MIR region. Monolayer BP has high band anisotropy, which gives rise to direction-dependent conduction. In addition, theoretical studies revealed that BP exhibits a puckered atomic structure, and the bandgap increases with an applied strain [140,141]. Therefore, the plasmonic dispersion in BP exhibits a strong dependence on the crystalline direction and strain [142,143]. This makes BP an interesting candidate for potential

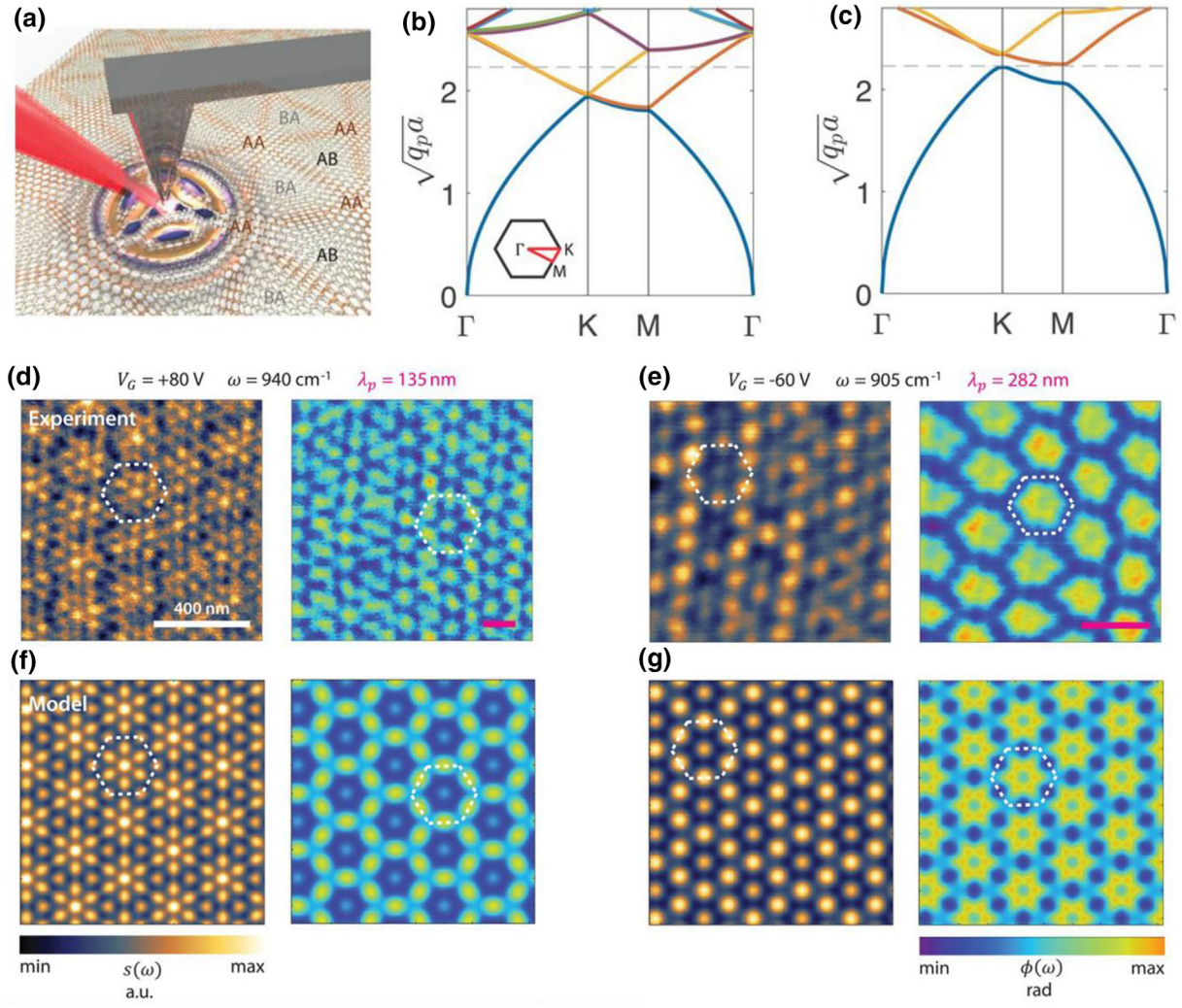

FIGURE 9

(a) Schematic of the IR near field nano-imaging setup. AA, AB and BA in the figure denotes different stacking type in TBG. (b) Calculated bandstructure based on the scattering strength (t = 0.02) obtained from experiment. (c) Calculated bandstructure based for a larger scattering strength (t = 0.2), which leads to a full bandgap. (d, e) Amplitude and phase of the plasmonic interference pattern obtained in experiment when the polariton wavelength is 135 nm and 282 nm respectively. The corresponding theoretical calculation using a superposition model are shown in (f) and (g). The white dash hexagon highlights the boundaries of a unit cell for the superlattice. Figures reproduced with permission from Ref. [126].

piezo-optic applications albeit it suffers from higher material loss [143].

Recently, Hu et al. reported the first observation of infrared plasmon polariton in $PtTe_2$, a type-II Dirac semimetal [144]. The plasmonic interference pattern between 1350 cm^{-1} to 2500 cm^{-1} is observed in $PtTe_2$ nanoribbons of different widths and thicknesses. To fully match the experimental plasmon dispersion of $PtTe_2$ nanoribbons, both a Drude model accounting for free electron motions and a Lorentz model accounting for the gapped intraband plasmons of Dirac fermion must be considered.

Two-dimensional polar crystals support MIR phonon polaritons, which have high confinement, small material loss, and thickness-dependent polariton dispersion [145,146]. These properties allow these crystals to be potentially used for building high-quality factor devices and polaritonic circuitry. Moreover, the 2D materials can be easily assembled with other material systems, such as phase change materials (VO_2, GST) or other 2D materials (graphene), greatly broadening their application scope.

In 2014, S. Dai et al. reported the first direct imaging of phonon polaritons in hexagonal boron nitride (h-BN) (Fig. 11a) [147]. The authors recorded the real space phonon polariton interference patterns using different excitation frequencies in the upper Reststrahlen band (1360 cm^{-1} to 1610 cm^{-1}). Fig. 11-b-g demonstrated that the polariton field patterns of a 256 nm thick h-BN crystal at different excitation frequencies. Measurement results could be accurately modeled by theoretical calculations as shown in Fig. 11h. Fig. 11i and j show higher-order polaritonic modes in both upper and lower Reststrahlen bands [148]. The authors also show the wavelength of PhPs scales inversely with the thickness and recent work demonstrates that such scaling law is valid until the monolayer limit [149]. Boron nitride is the first demonstrated natural 2D material that shows hyperbolic dispersion. This unique property turns the isofrequency contour of light into a hyperboloid and enables a range of

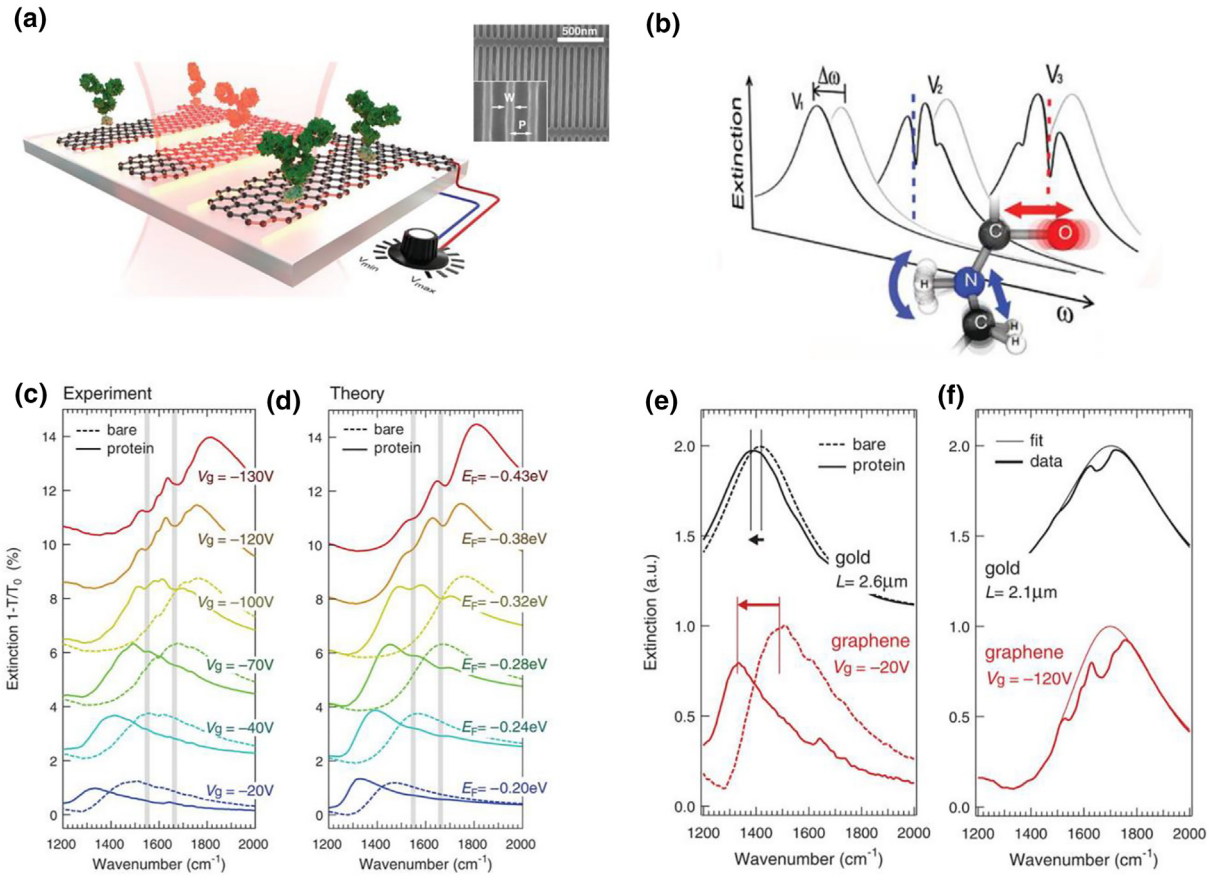

FIGURE 10

(a) Conceptual view of the tunable graphene MIR biosensor. The upper right inset shows a SEM image of the graphene nanoribbons with width $W = 30$ nm and period $P = 80$ nm. Vertical nanoribbons are electrically interconnected by horizontal strips. (b) Protein sensing is achieved by detecting a plasmon resonance spectral shift ($\Delta\omega$) accompanied by narrow dips corresponding to the molecular vibration bands of the protein. (c)–(d) Measured and calculated extinction spectra of the graphene sensor with (solid curves) and without (dashed curves) the protein, for different Fermi levels. Gray vertical strips indicate amide I and II vibrational bands of the protein. (e) Extinction spectra of biosensors using graphene plasmon and gold nanorod plasmon. Here the molecular vibration bands are away from the plasmonic resonance. The spectral shift of the plasmonic resonance (indicated by horizontal arrows) shows the refractive index sensitivity of the biosensors. The gold nanorod have dimensions 2.6 μm × 0.2 μm × 0.1 μm while the graphene is biased to $V_g = -20$ V. (f) Extinction spectra of the graphene and gold biosensors when the plasmonic resonance peak overlaps with the molecular vibration bands. The length of the gold nanorod was reduced to 2.1 μm to move its plasmonic resonance peak to this higher energy. The graphene biosensor is the same as that used in (e), only the gate voltage was changed to $V_g = -120$ V. The intensity of the spectral features at amide I and II bands (1660–1550 cm^{-1}) indicates the SEIRA sensitivity of the biosensors. The inset shows the schematic of the gold nanorod biosensor. Figures reproduced with permission from Ref. [137].

unconventional photonic phenomena, such as negative refraction [150], super-resolution optical imaging [148,151], strong light-matter interaction [152], etc. The recently discovered 2D materials such as α-MoO_3 [153,154] and α-V_2O_5 [155] are biaxial polar crystals. Hyperbolic dispersion appears in the plane orthogonal to the c-axis and these materials could be treated as natural hyperbolic metasurface. Some theoretical analyses predicted that nanostructured graphene and black phosphorus gratings also exhibit hyperbolic dispersion properties [156,157], but no experimental demonstration is reported up to today. Recent works from Basov's group revealed that photoexcited carriers in WSe_2 can cause different effects on its in-plane and out-of-plane permittivity, which proved that it is possible to create a photoinduced hyperbolic state for a few picoseconds [158].

Researchers have been exploiting the possibilities of designing phonon-based photonic devices working in the MIR, such as deep subwavelength, high-quality factor resonators [159–161]. An interesting research trend recently has been to integrate phonon materials with other material systems, such as VO_2 and GST or germanium [162–165]. Fig. 12a shows a hybrid device comprised of a thin layer of h-BN deposited on top of GST. The phase of GST can be reversibly switched between amorphous and crystalline by writing with laser pulses of different energy and durations, as shown in Fig. 12b. Since the material exhibits different refractive indices in different phases, the effective index of the polariton mode could be tailored by altering the phase of GST locally. Different 2D optical components could be written and erased on the film by selectively switch the GST's phase. Fig. 12-c-g indicate the process of writing and erasing different polaritonic devices using laser pulses. The corresponding near field image of the polariton field is illustrated in Fig. 12(h–k). The convex lens shows clear focusing of PhPs and it can be erased and turned into a concave lens. Using similar concepts as metamaterials, writing rod arrays of different spacings or different lengths could be used to engineer the phase of polaritons after passing through the rod arrays. A 2D metalens for phonon polariton is designed and characterized in this work. Strong coupling between phonon polariton in h-BN and the molecular vibra-

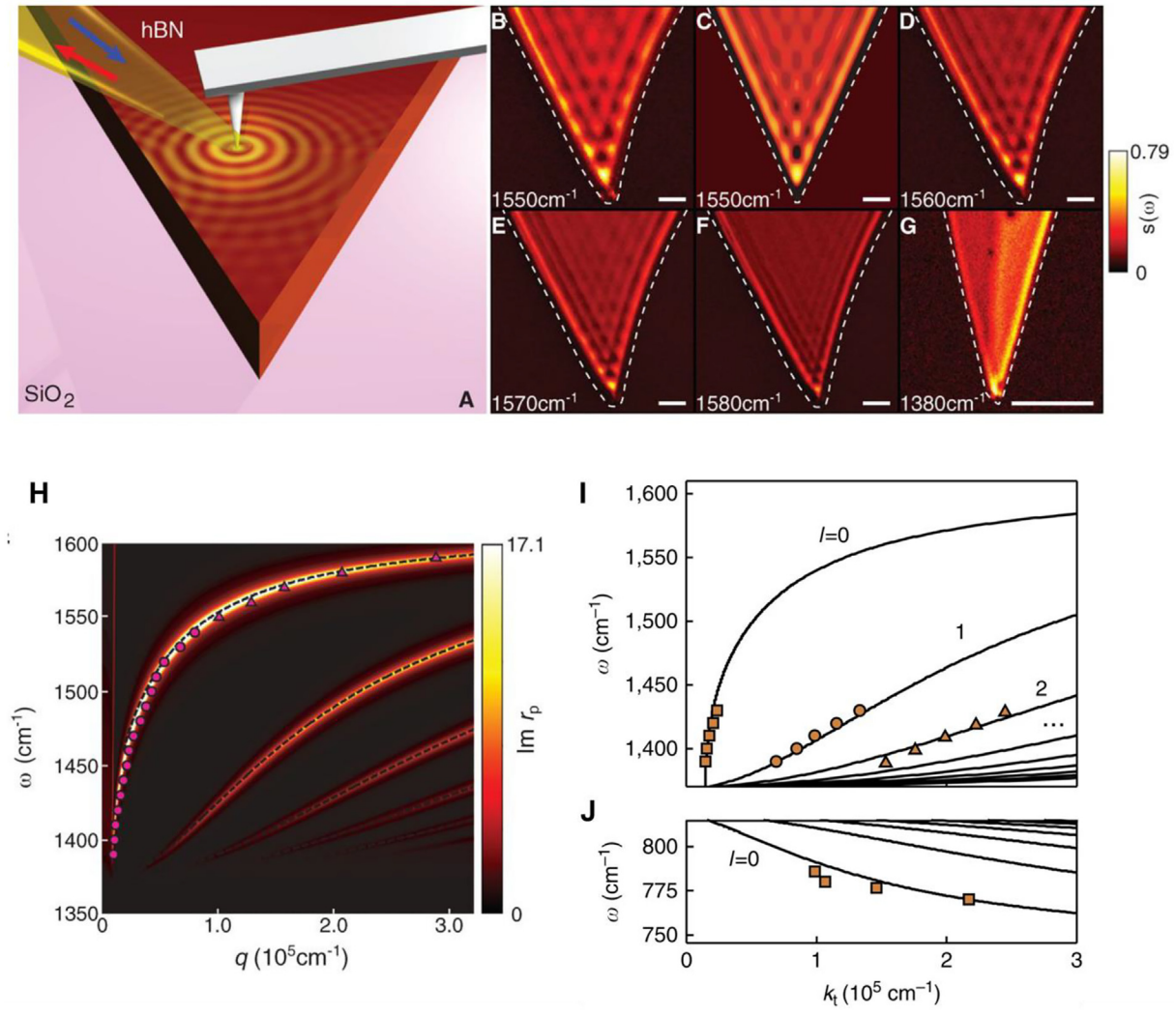

FIGURE 11

(a) Schematics of the near field IR nanoimaging setup. (b, d–f) Magnitude of the scattered near field signal s(ω) at 1550 cm^{-1}, 1560 cm^{-1}, 1570 cm^{-1} and 1580 cm^{-1}. The thickness of the h-BN crystal is 256 nm. (c) The simulated phonon polariton interference pattern at 1560 cm^{-1} for h-BN of the same thickness. (g) Real space mapping of the phonon polariton for h-BN of 3-layer (left) and 4-layer (right) at 1380 cm^{-1}. The white dash lines highlight the boundaries of h-BN crystal. (h) Dispersion relation of phonon polariton for a 256 nm thick h-BN. The triangle are data points extracted from near field mapping in (b, d–f). Dashed lines are nano-FTIR results. The background false-color plot are calculated imaginary part of the reflection coefficient r_p. (i, j) Dispersion results showing the first several orders of phonon polariton modes in upper and lower Reststralen bands. Square, circle and triangles denote zero order, first order and second order respectively. Figures are reproduced with permission from Refs. [147] and [148].

tional mode in organic molecules suggested that thin films of organic molecules could modify the polariton dispersions [166]. Therefore, by analyzing the polariton properties (wavelength, group velocity and loss, etc), an ultrasensitive on-chip spectroscopy could be realized.

Hybridizing graphene plasmons polaritons and phonon polaritons paves a way to simultaneously achieve high confinement, low propagating losses, and electrical tunability [167–173]. In 2014, Brar et al. performed MIR transmission measurements to reveal the hybridization of graphene plasmons and the phonons in a monolayer h-BN sheet, which creates two new surface-phonon-plasmon-polariton (SPPP) modes with dispersion relations that are distinctly different from the original graphene plasmon dispersion. Dai et al. reported the first direct near-field observation of the SPPP waves on graphene/h-BN heterostructure [168]. It has been shown both theoretically and experimentally that 2D materials such as atomically-thin transition metal dichalcogenides on silicon carbide polar substrate can be used as a system to support low-loss ultra-confined (190-times confinement) SPhPs [174]. Heterostructures comprised of anisotropic black phosphorus and isotropic h-BN are shown to create an in-plane anisotropic phonon polariton for h-BN and the degree of anisotropy could exceed that of a bare BP crystal [175].

Non-equilibrium photo-induced plasmons were observed with similar graphene/h-BN structures [173]. Plasmons can be activated with femtosecond optical pulses in such a graphene layer that lacks infrared plasmonic response at equilibrium. This femtosecond photo-switching of surface plasmon has also been demonstrated in BP heterostructures [176]. In a SiO_2/BP/SiO_2 heterostructure, the surface phonon modes of the SiO_2 layers hybridize with surface plasmon modes in BP that can be activated by photo-induced interband excitation. The free carriers

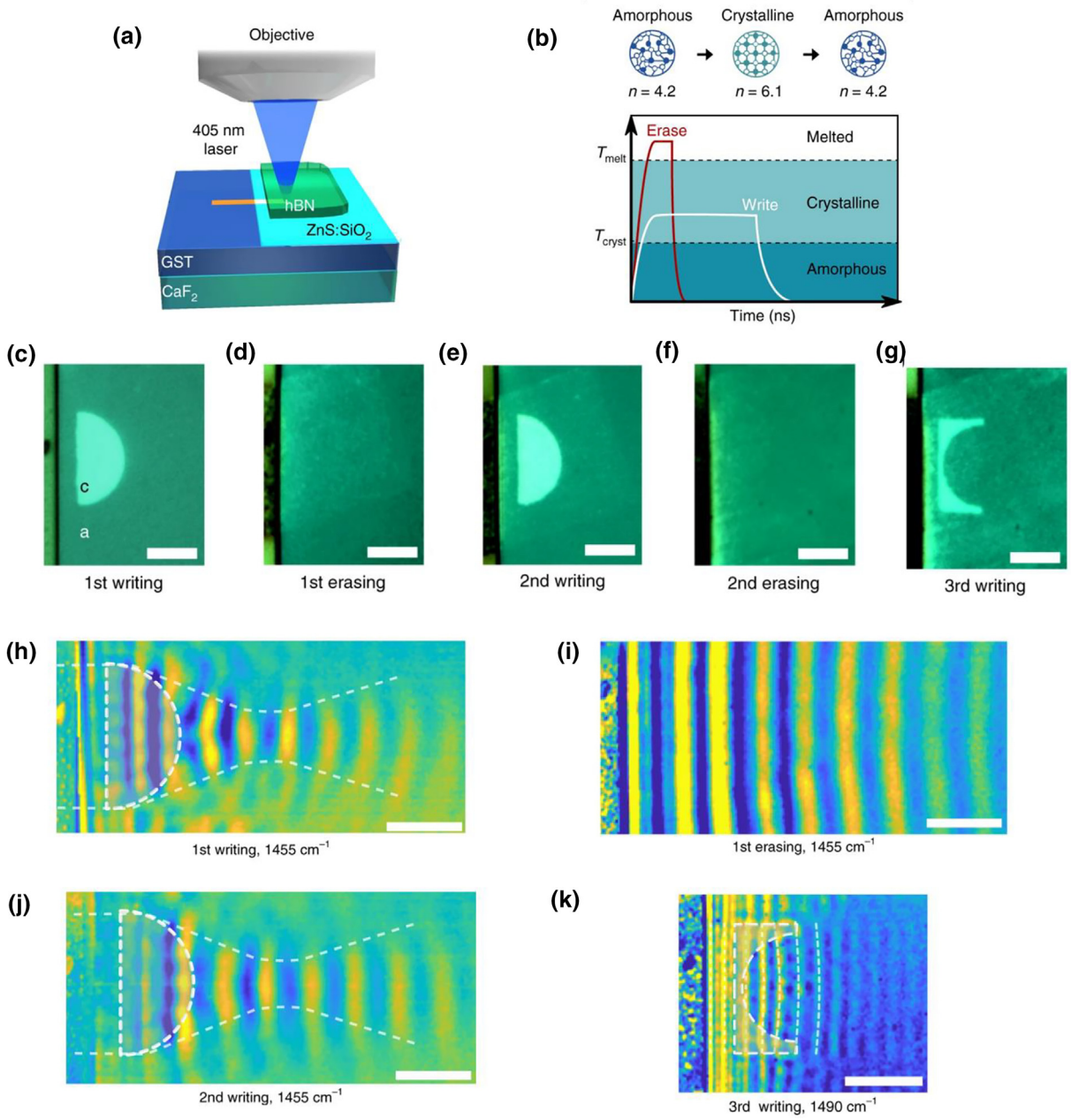

FIGURE 12

(a) Schematics of the reconfigurable device structure and writing setup. A 405 nm laser is used to write and erase patterns on the GST film beneath h-BN. (b) Writing and erasing process in GST. A longer, lower power pulse is used to induce a phase change in GST from amorphous to crystalline. A shorter, high-power pulse is used to melt the material and turn it into amorphous. The refractive indices of amorphous and crystalline phase are 4.2 and 6.1 respectively. (c–g) The process of writing and erasing different planar optical devices on GST film. The written image is clearly visible because the difference in refractive index between amorphous phase and crystalline phase. (h–k) The near field imaging of the phonon polariton after each stage of writing, erasing and rewriting. Clear focusing effect and reconfigurable property is demonstrated. The scale bar equals 5 μm. Figures reproduced with permission from Ref. [163].

generated by the ultrafast near-IR pump laser define a plasma frequency in the MIR. Consequently, the scattered near-field intensity of the MIR probe pulses is strongly modified when the near-field tip is located over the BP sample.

Nonlinear optical properties of 2D materials

Harmonic generation and frequency mixing

Nonlinear optical processes are crucial in a variety of applications in which the nonlinearities of 2D materials and their efficiency, tunability are the main figure-of-merits. For instance, optical parametric amplification based on $\chi^{(2)}$ or $\chi^{(3)}$ nonlinearity enables the generation of broadly tunable lasers [177]. Four-wave-mixing ($\chi^{(3)}$ nonlinearity) is also used for frequency comb and soliton generation [178], while high harmonic generation enables one to create extreme ultraviolet light [179] and attosecond pulse [180]. Compared to conventional nonlinear crystals, 2D materials could significantly modify the nonlinear responses, e.g., the emergence of even-order harmonics which do not exist in the bulk crystal [181–184], access to individual valleys [185,186], enhanced many-body interactions [187–190], and

dependence on the ellipticity of the excitation light [191]. Two-dimensional materials usually have much larger nonlinearities [192–197]. Moreover, the potential to electrically control the nonlinear response by a gate voltage is an additional important advantage, which may lead to compact nanophotonic devices for new applications in optical signal processing and on-chip ultrafast light generation. General reviews on perturbative nonlinear optical properties of 2D materials can be found elsewhere [198,199]. Here, we will mainly focus our discussions on their nonlinear responses in the MIR region.

In 2007, Mikhailov predicted that the unique cone-like linear, massless band structure of graphene will lead to strong nonlinearities, resulting in the generation of odd-order harmonics of the excitation optical wave [200]. The harmonic frequency can vary from microwaves up to infrared, and the amplitude of the excitation field is rather low, especially at low carrier densities and low temperatures (several hundred $V{\cdot}cm^{-1}$) [201]. The absence of even-order harmonics is due to the centrosymmetry of the graphene's crystal structure [202]. Third-order nonlinearities $\chi^{(3)}$ in graphene has latter been experimentally investigated, exhibiting a value up to 1.5×10^{-7} esu for a single graphene layer in the near-infrared, which is expected to grow significantly in longer wavelengths [203–206]. The value of $\chi^{(3)}$ here is 8 and 2 orders of magnitude larger than that in glasses and gold, respectively. The giant $\chi^{(3)}$ in graphene was also be experimentally verified in the MIR regime (~2 μm wavelength) using a Z-scan technique [207]. Broadband, electrically tunable third-harmonic generation in graphene was realized by Soavi et al., which can be modulated by over one order of magnitude by controlling the Fermi level [208]. The THG signal could be increased by three orders of magnitude when a graphene-insulator–metal structure is exploited [209]. The tuning of graphene plasmon by electrostatic gating can mediate the optical nonlinearity and modifies THG accordingly.

Second-harmonic generation (SHG) in ideal graphene is forbidden due to the space inversion symmetry. However, strong SHG can alternatively be observed when the space inversion symmetry is broken. The approaches include applying a direct current (DC) across the graphene [210–212], placing the graphene on some polar substrates (such SiO_2 and SiC) [213–215], using bilayer graphene with small twisting angles [216,217], and taking advantage of the long-range curvature fluctuations on suspended graphene [218]. Wu et al. predicted a giant and tunable resonance-enhanced $\chi^{(2)}$ of AB-stacked bilayer graphene (BLG) in the MIR region [212]. Fig. 13a shows the schematic of the BLG field-effect transistor used in the study. An in-plane current flows across the BLG and tilts the Fermi surface in the band structure, as illustrated by the tilted dash line in Fig. 13d. The tilted Fermi surface breaks the symmetry of the optical transition at opposite momenta (+k and −k) so that a nonzero second-order nonlinear optical conductivity σ_2 is obtained ($\chi^{(2)}$ is proportional to σ_2). Fig. 13b and c indicate the real and imaginary parts of σ_2^x as a function of the incident laser frequency, which are greatly enhanced at the resonant frequencies (1) ω = 0.4 eV and (2) ω = 0.2 eV. In the former case, all the optical transition intermediate states are real states (Fig. 13d), giving rise to the so-called double resonance-enhanced harmonic generation. The authors also showed that the SHG in BLG can be controlled by tuning the DC in-plane current, Fermi level, or the electronic bandgap. Fig. 13e shows the tunable $|\sigma_2|$ by controlling the bandgap (Δ) of BLG at 180 K. The resonant wavelengths for SHG in BLG are electrically tunable from ~5 to ~6 μm and from ~2.6 to ~3.1 μm. In 2020, Y. Zuo et al. reported a method to directly grow transition metal dichalcogenides (MoS_2) onto a hollow capillary fiber and a photonic crystal fiber [219]. They observed a 300-times enhancement of SHG/THG signal strength compared to the signals obtained from a monolayer MoS_2 on fused silica substrate. With these TMDs-coated fibers, they demonstrated all-fiber mode-lock laser with ~6 mW output power and 500 fs pulse width.

The nonlinear process discussed above is in the perturbative (weak field) regime, characterized by rapidly decreasing efficiency with increasing harmonic order. Therefore, usually only second and/or third-order nonlinearities are observable. In the strong field regime, where the electric field from the laser is not negligible compared to the electric field in atoms, the non-perturbative nature allows for high-order harmonic generation [220]. As the maximum photon energy scales with λ^2, MIR excitation is desirable [221]. Previously, efficient high harmonic generation (HHG) had been limited to atomic and molecular gases. Recently, the observation of HHG in bulk solids has attracted much attention [221–224], as it has opened a new platform for exploiting the atto-science and carries the possibility of realizing more compact and brighter extreme ultraviolet sources [225]. Yoshikawa et al. observed odd-order harmonics up to ninth order in monolayer graphene with an excitation wavelength of 4.77 μm and a peak laser intensity of 1.7 TW/cm^2 [191]. The authors showed that the high-harmonic generation can be enhanced with certain elliptically polarized excitation if the material is in the semimetal regime, which can be realized in graphene easily. These findings verify a theoretical framework previously developed by the same group [226,227]. Simultaneously, Liu et al. demonstrated non-perturbative HHG in monolayer MoS_2, with even and odd harmonics extending the 13th order, using a 4.13 μm MIR pump with 2.2 TW/cm^2 peak intensity [184]. The authors observed an enhanced HHG efficiency as compared to the bulk MoS_2 crystal, which can be attributed to the much stronger electron-hole Coulomb interactions in monolayer MoS_2, as a consequence of reduced dielectric screening in the atomically thin layer [188,189,228]. N. Yoshikwa et al. demonstrated the HHG in monolayer TMDs up to 18th order the signal of the even order harmonics are resonantly enhanced due to the band nesting energy [229]. The mechanism of HHG in solids is fundamentally different from that in atomic gases because of the higher density of atoms and their periodic structure [224]. The main restriction of HHG in solids is the relatively low maximum light intensity, limited by their damage thresholds. Solid materials also exhibit a less favorable scaling of the maximum HHG photon energy with the pump intensity [221] and wavelength [225]. Therefore, HHG sources based on solid-state materials are not yet able to compete with their atomic gas counterparts. However, Dejean et al. theoretically demonstrated that it is possible to circumvent all these limitations in a free-standing monolayer if the electrons are driven out of the plane by the external electrical field, which can be realized by using a pump laser with grazing incidence [225]. Breton et al. extended the work by investigating how the

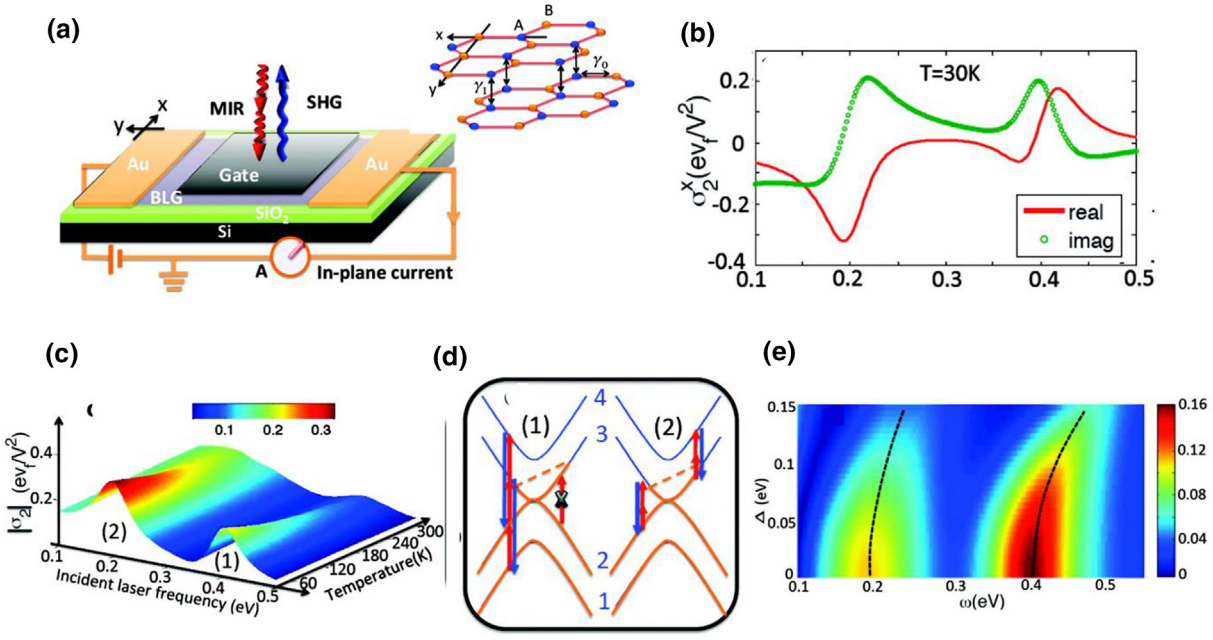

FIGURE 13

(a) Schematic of the bilayer graphene FET device with a dual-gated configuration so that the Fermi level and bandgap of BLG can be tuned separately. (b) Frequency dependent second order optical conductivity under circularly under left-hand circularly polarized light excitation, calculated at a temperature of 30 K. (c) second order optical conductivity as a function of temperature and laser frequency. (d) Corresponding nonlinear optical process for the response peak at (1) ω = 0.4 eV and (2) ω = 0.2 eV. (e) Tunable $|\sigma_2|$ by controlling the bandgap (Δ) of BLG at 180 K. The black dashed lines denote the resonant frequencies. Figures reproduced with permission from Ref. [212].

in-plane and out-of-plane HHG from h-BN evolve from monolayer to bulk [230].

2D materials MIR saturable absorption for mode-locked and Q-switched lasers

The optical absorption of 2D materials usually stems from the excitation of electron-hole pairs by incident light. At high excitation intensity, the concentration of these photogenerated carriers (electrons and holes) could be much higher than the intrinsic carrier densities, causing the states near the transition energy to be filled, and, thus, blocking further photon absorption [231,232]. This Pauli blocking leads to saturable absorption, widely used in ultrashort optical pulse generation.

The study of saturable absorption properties of 2D materials was first carried out in graphene [231]. Compared to the widely used single-walled carbon nanotubes (SWNTs) and semiconductor saturable absorber mirrors (SESAMs), graphene is superior in the following aspects: (1) relatively large and broadband light absorption (2.3% per layer for a wide spectral range while SWNTs and SESAMs are narrowband although a mixture of SWNTs with different diameters could provide a broader absorption [233]); (2) ultrafast carrier recombination (within 10–150 fs, [234] typically an order of magnitude shorter than that of SWNTs [235]). All these imply that graphene can be a fast saturable absorber for broad bandwidth. Experimental demonstration of graphene mode-locked laser was first reported in 2009 at ~1.5 μm wavelength, taking advantage of the readily available optical components in this well-developed region [231,232]. It was found that graphene saturable absorber has a one-order-of-magnitude lower saturation intensity and 2–3 times larger modulation depth than SWNTs and SESAMs [231]. The larger modulation depth stems from the much smaller non-saturable loss of graphene and can be further enhanced by stacking multiple layers of graphene. These unique properties of lower saturation intensity, ultrafast recovery time, tunable modulation depth, and broadband feature suggest that graphene films are promising and universal saturable absorbers for mode-locked pulse generation in a wide spectral range. Saturable absorption of graphene can also be enhanced by increasing interlayer coupling of layered 2D materials. For example, the interlayer coupling in the graphene/WSe_2 heterostructure can enhance the saturable absorption [236]. In this case, graphene serves as a fast channel for the relaxation of the photoexcited electrons in WSe_2, and the nonlinear absorption of WSe_2 could be effectively tuned by the carrier transfer process in graphene, enabling specific optical absorption of the heterostructure in comparison with separated graphene or WSe_2.

Since the first work in 2009, graphene mode-locking has been realized in a wide variety of gain media with numerous configurations, in the near-infrared wavelengths. In the MIR region, Ma et al. first demonstrated a graphene mode-locked Tm: CLNGG laser at 2 μm using a chemical-vapor-deposited (CVD) graphene transferred onto a highly reflective plane mirror [237]. They obtained stable mode-locked pulses with 729 fs duration and 60.2 mW average power. Later, graphene mode-locked lasers were realized in Tm: Lu_2O_3 [238], Cr: ZnSe [239,240], Cr: ZnS [241–243], Tm: YAG Ceramic [244], and Er^{3+}-doped ZBLAN fiber [245], covering the 2.0–2.5 μm and 2.8 μm wavelengths. The highest average power and pulse energy are 880 mW [243] and 15.5 nJ [241], respectively. In 2014, Ma et al. also demonstrated the ultra-broadband mode-locking performance of the same

graphene-gold saturable absorber mirror at 1 μm, 2 μm and 2.4 μm using Yb: YCOB, Tm: CLNGG and Cr: ZnSe crystals, respectively, as the laser gain medium in the same laser configuration [239], verifying the ultra-broad saturable absorption nature of graphene.

Graphene saturable absorbers have achieved great research success, both in the near-IR and MIR wavelengths. However, there are also some limitations. For example, the damage threshold of graphene saturable absorber in MIR is up to 1 mJ/cm^2 [241], compared to 4 mJ/cm^2 for the commercial 2 μm SESAM (Batop GmbH, Germany). This would limit their application in high-power lasers. Currently, some of the research efforts are put into pushing the power level of the MIR graphene mode-locked laser to watt level (watt level mode-locked laser with graphene has already demonstrated in near-IR [246]). Another major concern on graphene saturable absorbers is their reliability or stability. As no systematic investigation in this aspect has been reported so far. Apart from graphene, other 2D materials also exhibit saturable absorption in MIR. Such as graphene oxide [247] and BP [248,249]. Table 3 summarizes the reported works on 2D materials mode-locked lasers in the MIR region.

On the other hand, MIR Q-switched lasers have been frequently reported with 2D materials as saturable absorbers, which give large pulse energy with long pulse duration from nanoseconds to microseconds and moderated peak power [250]. Stable pulse duration of 2.9 μs and pulse energy of 1.67 μJ was achieved in a diode-pumped 2.78 μm fiber laser where graphene was applied onto the fiber dichroic mirror as a saturable absorber [251]. The low modulation depth of graphene Q-switched lasers originating from the weak absorption can be overcome by introducing other 2D materials with suitable band gap and optical absorption coefficients. For example, Qin et al. [252] reported Q-switched Er:ZBLAN fiber laser at 2.8 μm with multilayer black phosphorus as the saturable absorber, exhibiting a maximum average power of 485 mW with corresponding pulse energy of 7.7 μJ and pulse width of 1.18 μs at a repetition rate of 63 kHz. However, black phosphorene is quite unstable due to its oxidation under ambient conditions. It degrades within hours, especially for the monolayer or few-layer 2D material samples in common fiber laser setups. This oxidation would be further accelerated under thermal effects in the presence of water, oxygen with high-pulse laser irradiation. The wavelength of the Q-switched laser could be extended by employing narrow bandgap 2D materials [253]. NiS_2 was employed as a saturable absorber and achieved nanosecond passively Q-switched fiber laser in both Erbium-doped fiber laser (EDFL) and Thulium-doped fiber

TABLE 3

Summary of 2D material mode-locked lasers in the MIR wavelength region.

Laser gain medium	Wavelength (nm)	Pulse width (fs)	Saturable absorber	Average power/Pulse energy	Remarks and year	Ref.
Tm: CLNGG	2018	729 fs	CVD graphene on dielectric-coated mirror	60.2 mW/ 0.61 nJ	First graphene mode-locked laser above 2 μm (2012)	[237]
Tm: CLNGG	2010	354 fs	CVD graphene on gold mirror	97 mW/ 0.99 nJ	(2014)	[239]
Tm:Lu_2O_3	2067	410 fs	CVD graphene on quartz substrate	270 mW/ 2.45 nJ	High power (2013)	[238]
Cr: ZnSe	2500	226 fs	CVD graphene on CaF_2 substrate	80 mW/ 1.04 nJ	(2013)	[240]
Cr: ZnSe	2310–2426	116 fs	CVD graphene on gold mirror	66 mW/ 0.67 nJ	Wavelength tunable (2014)	[239]
Cr: ZnS	~2400	41 fs	CVD graphene on DBR	250 mW/ 2.3 nJ	Shortest pulses generated in the MIR, as well as the shortest pulses obtained with the graphene SA (2014)	[242]
Cr: ZnS	~2350–2450	870 fs	CVD graphene on DBR	700 mW/ 15.5 nJ	First solid-state dissipative soliton laser ever mode-locked by graphene with high-energy pulse (2014)	[241]
Cr: ZnS	2120–2408	220 fs	CVD graphene on CaF_2 substrate	880 mW/ 7.8 nJ	Tunable graphene mode-locked solid-state laser with broadest spectral tuning range (2016)	[243]
Tm: YAG Ceramic	2016	2.8 ps	CVD graphene on gold mirror	158 mW/ 1.6 nJ	Shortest pulse generated from mode-locked Tm: YAG lasers (2015)	[244]
Er^{3+}-doped ZBLAN fiber	2784	~4.2 ps	CVD graphene on gold mirror	18 mW/ 0.71 nJ	First demonstration of mode-locked operation of an Er^{3+}-doped ZBLAN fiber laser using graphene (2016)	[245]
Tm:$YAlO_3$ Crystal	2023	~10 ps	liquid phase exfoliation (LPE) graphene oxide on quartz	268 mW/ 3.7 nJ	First graphene oxide mode-locked laser above 2 um (2012)	[247]
Er^{3+}-doped ZBLAN fiber	2783	42 ps	Mechanically exfoliated black phosphorus on gold mirror	613 mW/ 25.5 nJ	First demonstration of black phosphorus mode-locked laser at 2.8 μm (2016)	[248]
Ho^{3+}/Pr^{3+} co-doped fluoride fiber	2867	8.6 ps	Liquid phase exfoliation (LPE) black phosphorus on gold mirror	87.8 mW/ 6.28 nJ	(2016)	[249]
Er:ZBLAN fiber	3500	ps	Liquid phase exfoliation (LPE) black phosphorus on gold mirror	40 mW/	First demonstration of SA beyond 3 um (2018)	[278]

laser (TDFL) cavities [254]. Few-layer platinum diselenide, a newly discovered narrow band gap 2D material, with a modulation depth of 7% and a saturation intensity of 25 GW/cm^2, was demonstrated as the saturable absorber in Nd:YVO_4 at 1.3 μm [255]. The maximum Q-switched pulse average power was 209 mW under the absorbed pump power of 3.62 W. Alternatively, Tian et al. [256] demonstrated solution-processed BiOSe as an ultra-broadband saturable absorber for the MIR, Q-switched laser, showing picosecond response and response amplitude up to ~330.1% at 5.0 μm. Another 2D material, antimonene, which has high stability, high carrier mobility and large thermal conductivity, was successfully employed as a long-term stable saturable absorber in a linear-cavity Ho^{3+}/Pr^{3+}-codoped fluoride fiber laser at about 2.9 μm [257]. Q-switched pulse laser was obtained under ambient conditions with a maximum output power of 112.3 mW and pulse energy of 0.72 μJ, while the shortest pulse duration and largest repetition rate were 1.74 μs and 156.2 kHz. Recently, antimonene-based saturable material was applied in Er:ZBLAN fiber laser for mid-infrared Q-switched pulse generation operating in the 2.8 μm regime with an output power of 59 mW corresponding to the pulse energy of 1.03 μJ [258]. Among various 2D materials, MXene has attracted attention on account of its distinct optical, electronic, and mechanical performances, especially high stability and damage threshold under pulse laser irradiation [259]. For instance, $Ti_3C_2T_x$ was demonstrated as an efficient saturable absorber in PQS Er^{3+}:CaF_2-SrF_2 laser at 2.83 μm [260]. The above intriguing reports indicate that low cost, easy fabrication, and variable bandgap of various 2D materials make them potential as a broadband saturable absorber for pulsed lasers, especially in the MIR spectral regime where few saturable absorbers can work stably.

Conclusions and outlook

Recent years have witnessed the rapid evolvement of 2D materials in photonic and optoelectronic technologies. In this review, we have discussed recent developments of 2D materials applied in the MIR spectral region.

From the viewpoint of fundamental research, the 2D material family provides an intriguing platform for exploiting new physics, chemistry, and material sciences. Many exotic phenomena have been predicted and observed over the years. In the field of optics, examples include the strong optical absorption of graphene in the infrared limit defined solely by the fine structure constant [261], the ultra-strong light confinement of the intrinsic surface plasmon [119], the high carrier mobilities enabling efficient and fast photodetection and optical modulation, the high intrinsic nonlinearity, etc. New fundamental questions also have been frequently raised, especially about their light-matter interactions in the MIR region. For example, the effects of the boundaries and edges of the atomic membranes on the photonic properties [192], the possibility of enhancing the nonlinear responses of 2D material with their intrinsic plasmon [262], etc. Recent theoretical works suggest that the out-of-plane nonlinear response of 2D materials is similar to those of atomic and molecular gases, while the in-plane nonlinear response may resemble bulk solids [225,230]. Achieving single-photon detection/emission and single molecular gas sensing with 2D materials would be another exciting perspective, which would underpin a host of applications at the frontiers of science and engineering, including remote sensing, medical imaging, and quantum information processing.

A vital link between fundamental research and practical applications is the accessibility of high-quality and large-area 2D materials. For MIR applications, material properties such as absorption/reflection and plasmon resonance are originated from the electronic atomic structure and carrier density of the materials. The emergence of stacking atomically thin layered 2D materials, such as graphene, black phosphorus (BP), tellurium (Te) and platinum diselenide ($PtSe_2$), through weak van der Waals (vdW) interactions, introduces a promising solution to the bottlenecks encountered by current MIR optoelectronics. Although 2D materials exhibit unique and promising properties in various aspects, many of which can only be achieved in intrinsic or high-quality 2D materials [263]. Mechanically exfoliated flakes from natural and artificial crystals synthesized by chemical vapour transport (CVD) method usually exhibit good quality, but they have a very limited size and are not suitable for massive production [74]. Large CVD-grown films, which is suitable for scalable fabrication, are usually much inferior to the intrinsic materials due to the impurities and defects introduced during the growth [14]. Alternative material production methods, such as physical vapour deposition (PVD) [11], molecular beam epitaxy (MBE) [264], and metal organic vapour epitaxy (MOCVD) [265], have been actively pursued in recent years to fulfill the requirements of MIR applications and beyond.

In the viewpoint of applications, it has been shown that 2D materials have promising applications in the important but less mature MIR spectral region due to the lack of suitable narrow bandgap materials. Many key building blocks for MIR technology have been established based on 2D materials, including plasmonic waveguides, photodetectors, modulators, optical sensors and non-linear optical elements [266]. Future development may lead to fully functional compact on-chip systems incorporating some or all these elements. However, while encouraging device performance has been demonstrated, 2D materials are not yet ready for replacement of the existing MIR materials. One could envision some challenges before 2D materials can become a truly competitive and widespread platform for MIR applications. These include (i) Reliability of the devices. The properties of the 2D materials are sensitive to the fabrication process and the surrounding environment, which has a significant impact on the performance and reproducibility of the devices. After fabrication, 2D materials may degrade over time in ambient environments due to humidity or contamination. Although this can be partially solved by encapsulating the 2D materials, the lifetime of the devices remains an issue and requires further investigation [266]. Additionally, detectors and optical modulators based on 2D materials often show undesirable hysteresis, which may be an issue in practical applications, although in some cases, such as optical memory, it can be a useful feature [267]. (ii) Cost of 2D material-based devices. The development of 2D materials has been at a rapid pace, with exciting discoveries emerging frequently. This gives the confidence that, despite all the lingering issues, future advances in this field will bring 2D materials to a new level of maturity, from fundamental science

discoveries to widespread real-world applications, especially in the MIR region.

Declaration of Competing Interest

The authors declare that they have no known competing financial interests or personal relationships that could have appeared to influence the work reported in this paper.

Acknowledgements

G. Liang and X. Yu contribute equally to this work. This work is support by funding from the Ministry of Education, Singapore grant (MOE2018-T2-1-176), A*Star AME programmatic grant under grant no. A18A7b0058, and National Research Foundation Competitive Research Program (NRF-CRP18-2017-02 and NRF-CRP22-2019-0007).

References

[1] R. Soref, Nat. Photonics 4 (2010) 495–497.
[2] A. Hoffman, Nat. Photonics 6 (2012) 407.
[3] J. Hu, J. Meyer, et al., Opt. Mater. Express 3 (2013) 1571–1575.
[4] A. Rogalski, Reports Prog. Phys. 68 (2005) 2267.
[5] H. Li, H. Alradhi, et al., Adv. Funct. Mater. 28 (2018) 1705382.
[6] K.K. Choi, B.F. Levine, et al., Appl. Phys. Lett. 50 (1987) 1814–1816.
[7] D. Palaferri, Y. Todorov, et al., Nature 556 (2018) 85–88.
[8] A.D. Stiff-Roberts, J. Nanophotonics 3 (2009) 031607.
[9] K.S. Novoselov, A.K. Geim, et al., Science. 306 (2004) 666–669.
[10] A.K. Geim, K.S. Novoselov, Nat. Mater. 6 (2007) 183–191.
[11] W. Choi, N. Choudhary, et al., Mater. Today 20 (2017) 116–130.
[12] A. Dehzangi, J. Li, et al., Light Sci. Appl. 10 (2021) 17.
[13] E.A. Anyebe, I. Sandall, et al., Sci. Rep. 7 (2017) 46110.
[14] E. Kahn, M. Liu, et al., Mater. Today 37 (2020) 74–92.
[15] F. Bonaccorso, Z. Sun, et al., Nat. Photonics 4 (2010) 611–622.
[16] F. Xia, T. Mueller, et al., Nano Lett. 9 (2009) 1039–1044.
[17] G. Konstantatos, M. Badioli, et al., Nat. Nanotechnol. 7 (2012) 363–368.
[18] T. Mueller, F. Xia, et al., Phys. Rev. B 79 (2009) 245430.
[19] N.O. Weiss, X. Duan, NPG Asia Mater. 5 (2013) e74.
[20] M. Freitag, T. Low, et al., Nat. Photonics 7 (2013) 53–59.
[21] N.M. Gabor, J.C.W. Song, et al., Science 334 (2011) 648–652.
[22] Y. Nam, D.-K. Ki, et al., Nat. Phys. 13 (2017) 1207–1214.
[23] L. Ju, L. Wang, et al., Science 358 (2017) 907–910.
[24] J. Yan, M.H. Kim, et al., Nat. Nanotechnol. 7 (2012) 472–478.
[25] Z. Fei, G.O. Andreev, et al., Nano Lett. 11 (2011) 4701–4705.
[26] T.R. Zhan, F.Y. Zhao, et al., Phys. Rev. B 86 (2012) 165416.
[27] S. Thongrattanasiri, F.J. García de Abajo, Phys. Rev. Lett. 110 (2013) 187401.
[28] J. Chen, M. Badioli, et al., Nature 487 (2012) 77–81.
[29] Q. Guo, R. Yu, et al., Nat. Mater. 17 (2018) 986–992.
[30] J. Wei, Y. Li, et al., Nat. Commun. 11 (2020) 6404.
[31] Y. Yao, R. Shankar, et al., Nano Lett. 14 (2014) 3749–3754.
[32] X. Wang, Z. Cheng, et al., Nat. Photonics 7 (2013) 888–891.
[33] Q. Gao, J. Guo, J. Appl. Phys. 112 (2012) 84316.
[34] B. Deng, C. Ma, et al., Nat. Photonics 14 (2020) 549–553.
[35] V.R., M.R., N.R., V.M., T. Otsuji, Jpn. J. Appl. Phys. 48 (2009) 04C144.
[36] L. Jiao, L. Zhang, et al., Nature 458 (2009) 877–890.
[37] D. Wei, L. Xie, et al., Nat. Commun. 4 (2013) 1374.
[38] X. Li, X. Wang, et al., Science 319 (2008) 1229–1232.
[39] F. Sols, F. Guinea, et al., Phys. Rev. Lett. 99 (2007) 166803.
[40] M.Y. Han, B. Özyilmaz, et al., Phys. Rev. Lett. 98 (2007) 206805.
[41] F. Bonaccorso, A. Lombardo, et al., Mater. Today 15 (2012) 564–589.
[42] X. Yu, Z. Dong, et al., Nanoscale 8 (2016) 327–332.
[43] Y. Cao, V. Fatemi, et al., Nature 556 (2018) 80–84.
[44] Y. Cao, V. Fatemi, et al., Nature 556 (2018) 43–50.
[45] X. Yu, Y. Li, et al., Nat. Commun. 9 (2018) 4299.
[46] C.H. Liu, Y.C. Chang, et al., Nat. Nanotechnol. 9 (2014) 273–278.
[47] M. Freitag, T. Low, et al., ACS Nano 8 (2014) 8350–8356.
[48] M. Badioli, A. Woessner, et al., Nano Lett. 14 (2014) 6374–6381.
[49] K.K. Gopalan, D. Janner, et al., Adv. Opt. Mater. (2016) 1600723.
[50] J. Kim, H. Jang, et al., in: Conf. Lasers Electro-Optics, Optical Society of America, San Jose, California, 2016, p. SF2E.3.
[51] F. Xia, H. Wang, et al., Nat. Commun. 5 (2014) 4458.
[52] Y. Ma, B. Dong, et al., Adv. Opt. Mater. 8 (2020) 2000337.
[53] R. Peng, K. Khaliji, et al., Nano Lett. 17 (2017) 6315–6320.
[54] W.C. Tan, L. Huang, et al., Adv. Mater. 30 (2018) 1705039.
[55] Q. Guo, A. Pospischil, et al., Nano Lett. 16 (2016) 4648–4655.
[56] L. Li, J. Kim, et al., Nat. Nanotechnol. 12 (2016) 21–25.
[57] X. Chen, X. Lu, et al., Nat. Commun. 8 (2017) 1672.
[58] F. Xia, H. Wang, et al., Nat. Photonics 8 (2014) 899–907.
[59] T. Low, M. Engel, et al., Phys. Rev. B 90 (2014) 81408.
[60] S. Yuan, C. Shen, et al., Nano Lett. 18 (2018) 3172–3179.
[61] M. Long, A. Gao, et al., Sci. Adv. 3 (2017) e1700589.
[62] S. Yuan, D. Naveh, et al., Nat. Photonics (2021) 1–7.
[63] J. Bullock, M. Amani, et al., Nat. Photonics 12 (2018) 601–607.
[64] Y. Wang, G. Qiu, et al., Nat. Electron. 1 (2018) 228–236.
[65] M. Amani, C. Tan, et al., ACS Nano 12 (2018) 7253–7263.
[66] C. Shen, Y. Liu, et al., ACS Nano 14 (2019) 303–310.
[67] G. Jnawali, Y. Xiang, et al., Nat. Commun. 11 (2020) 3991.
[68] L. Tong, X. Huang, et al., Nat. Commun. 11 (2020) 2308.
[69] W. Wu, G. Qiu, et al., Chem. Soc. Rev. 47 (2018) 7203–7212.
[70] T.Q. Trung, N.T. Tien, et al., Adv. Mater. 24 (2012) 5254–5260.
[71] T.Q. Trung, S. Ramasundaram, et al., Adv. Funct. Mater. 25 (2015) 1745–1754.
[72] Y. Hu, P. Kumar, et al., Adv. Opt. Mater. 4 (2016) 1811–1823.
[73] X. Yu, P. Yu, et al., Nat. Commun. 9 (2018) 1545.
[74] K. Deng, G. Wan, et al., Nat. Phys. 12 (2016) 1105–1111.
[75] L. Huang, T.M. McCormick, et al., Nat. Mater. 15 (2016) 11–17.
[76] Y. Qi, P.G. Naumov, et al., Nat. Commun. 7 (2016) 11038.
[77] Y. Sun, S.C. Wu, et al., Phys. Rev. B 92 (2015) 161107.
[78] S. Jia, S.Y. Xu, et al., Nat. Mater. 15 (2016) 1140–1144.
[79] J. Liu, F. Xia, et al., Nat. Mater. 19 (2020) 830–837.
[80] Z. Ji, W. Liu, et al., Science. 368 (2020) 763–767.
[81] J. Wei, C. Xu, et al., Nat. Photonics 15 (2021) 614–621.
[82] S. Pirotta, N.-L. Tran, et al., Nat. Commun. 12 (2021) 799.
[83] N. Dabidian, S. Dutta-Gupta, et al., Nano Lett. 16 (2016) 3607–3615.
[84] B. Zeng, Z. Huang, et al., Light Sci. Appl. 7 (2018) 51.
[85] Y. Yao, R. Shankar, et al., Nano Lett. 14 (2014) 6526–6532.
[86] Z. Sun, F. Huang, et al., Opt. Commun. 474 (2020) 126115.
[87] K. Fan, J.Y. Suen, et al., Opt. Express 25 (2017) 25318–25325.
[88] N.K. Emani, T.F. Chung, et al., Nano Lett. 12 (2012) 5202–5206.
[89] N.K. Emani, T.F. Chung, et al., Nano Lett. 14 (2013) 78–82.
[90] Z. Fang, S. Thongrattanasiri, et al., ACS Nano 7 (2013) 2388–2395.
[91] Z. Fang, Y. Wang, et al., Nano Lett. 14 (2014) 299–304.
[92] V.W. Brar, M.S. Jang, et al., Nano Lett. 13 (2013) 2541–2547.
[93] H. Yan, T. Low, et al., Nat. Photonics 7 (2013) 394–399.
[94] J. Tao, X. Yu, et al., Opt. Lett. 39 (2014) 271–274.
[95] J. Lao, J. Tao, et al., Laser Photonics Rev. 8 (2014) 569–574.
[96] W. Luo, W. Cai, et al., Opt. Express 24 (2016) 5784–5793.
[97] H. Deng, Y. Yan, et al., IEEE Photonics Technol. Lett. 27 (2015) 1161–1164.
[98] H. Cheng, S. Chen, et al., Appl. Phys. Lett. 103 (2013) 203112.
[99] Z. Li, N. Yu, Appl. Phys. Lett. 102 (2013) 131108.
[100] Y. Yao, M.A. Kats, et al., Nano Lett. 13 (2013) 1257–1264.
[101] Y. Yao, M.A. Kats, et al., Nano Lett. 14 (2014) 214–219.
[102] S.H. Mousavi, I. Kholmanov, et al., Nano Lett. (2013) 1111–1117.
[103] J. Ding, B. Arigong, et al., Sci. Rep. 4 (2014) 6128.
[104] A.M. Aygar, O. Balci, et al., ACS Photonics 3 (2016) 2303–2307.
[105] N. Dabidian, I. Kholmanov, et al., ACS Photonics 2 (2015) 216–227.
[106] V. Tran, R. Soklaski, et al., Phys. Rev. B 89 (2014) 235319.
[107] C. Lin, R. Grassi, et al., Nano Lett. 16 (2016) 1683–1689.
[108] M. Liu, X. Yin, et al., Nature 474 (2011) 64–67.
[109] R.K. Schaevitz, E.H. Edwards, et al., IEEE J. Quantum Electron. 48 (2012) 187–197.
[110] W.S. Whitney, M.C. Sherrott, et al., Nano Lett. 17 (2017) 78–84.
[111] Y. Liu, K. Tom, et al., Nano Lett. 16 (2016) 488–496.
[112] S. Deckoff-Jones, Y. Wang, et al., ACS Photonics 6 (2019) 1632–1638.
[113] S. Zhang, T. Ma, et al., Mater. Today 26 (2019) 67–86.
[114] M.C. Sherrott, P.W.C. Hon, et al., Nano Lett. 17 (2017) 3027–3034.
[115] M.E.A. Panah, O. Takayama, et al., Opt. Express 24 (2016) 29077–29088.
[116] S. Law, V. Podolskiy, et al., Nanophotonics 2 (2013) 103–130.
[117] Y. Zhong, D. Wasserman, et al., J. Nanophotonics 9 (2015) 093791.
[118] T. Low, P. Avouris, ACS Nano 8 (2014) 1086–1101.
[119] F.J.G. De Abajo, ACS Photonics 1 (2014) 133–152.
[120] Z. Fei, A.S. Rodin, et al., Nature 487 (2012) 82–85.
[121] G.X. Ni, A.S. McLeod, et al., Nature 557 (2018) 530–533.
[122] A. Woessner, M.B. Lundeberg, et al., Nat. Mater. 14 (2014) 421–425.
[123] N.P. De Leon, B.J. Shields, et al., Phys. Rev. Lett. 108 (2012) 226803.

[124] M. Kuttge, F.J. García De Abajo, et al., Nano Lett. 10 (2010) 1537–1541.
[125] G.X. Ni, H. Wang, et al., Nat. Mater. 14 (2015) 1217–1222.
[126] S.S. Sunku, G.X. Ni, et al., Science. 362 (2018) 1153–1156.
[127] Z. Fei, A.S. Rodin, et al., Nat. Nanotechnol. 8 (2013) 821–825.
[128] G.X. Ni, H. Wang, et al., Nat. Commun. 10 (2019) 4360.
[129] G. Hu, Q. Ou, et al., Nature 582 (2020) 209–213.
[130] Z. Zheng, F. Sun, et al., Nano Lett. 20 (2020) 5301–5308.
[131] J. Duan, N. Capote-Robayna, et al., Nano Lett. 20 (2020) 5323–5329.
[132] M. Chen, X. Lin, et al., Nat. Mater. 19 (2020) 1307–1311.
[133] F. He, Y. Zhou, et al., ACS Nano 15 (2021) 5944–5958.
[134] F.H.L. Koppens, D.E. Chang, et al., Nano Lett. 11 (2011) 3370–3377.
[135] F. Liu, E. Cubukcu, Phys. Rev. B 88 (2013) 115439.
[136] Y. Li, H. Yan, et al., Nano Lett. 14 (2014) 1573–1577.
[137] D. Rodrigo, O. Limaj, et al., Science 349 (2015) 165–168.
[138] P. Li, T. Wang, et al., Nano Lett. 14 (2014) 4400–4405.
[139] A. Vakil, N. Engheta, Science 332 (2011) 1291–1294.
[140] A.S. Rodin, A. Carvalho, et al., Phys. Rev. Lett. 112 (2014) 176801.
[141] R. Fei, L. Yang, Nano Lett. 14 (2014) 2884–2889.
[142] T. Low, R. Roldán, et al., Phys. Rev. Lett. 113 (2014) 106802.
[143] K.T. Lam, J. Guo, J. Appl. Phys. 117 (2015) 113105.
[144] X. Hu, K.P. Wong, et al., ACS Nano 14 (2020) 6276–6284.
[145] J.B. Khurgin, Nat. Nanotechnol. 10 (2014) 2–6.
[146] J.B. Khurgin, G. Sun, Appl. Phys. Lett. 99 (2011) 211106.
[147] S. Dai, Z. Fei, et al., Science 343 (2014) 1125–1129.
[148] S. Dai, Q. Ma, et al., Nat. Commun. 6 (2015) 6963.
[149] S. Dai, W. Fang, et al., Adv. Mater. 31 (2019) 1806603.
[150] J. Jiang, X. Lin, et al., Research 2018 (2018) 2532819.
[151] P. Li, M. Lewin, et al., Nat. Commun. 6 (2015) 7507.
[152] M. Autore, P. Li, et al., Light Sci. Appl. 7 (2018) 17172.
[153] Z. Zheng, J. Chen, et al., Adv. Mater. 30 (2018) 1705318.
[154] W. Ma, P. Alonso-González, et al., Nature 562 (2018) 557–562.
[155] J. Taboada-Gutiérrez, G. àlvarez-Pérez, et al., Nat. Mater. (2020) 1–5.
[156] D. Correas-Serrano, J.S. Gomez-Diaz, et al., J. Opt. 18 (2016) 104006.
[157] J.S. Gomez-Diaz, A. Alu, ACS Photonics 3 (2016) 2211–2224.
[158] A.J. Sternbach, S.H. Chae, et al., Science. 371 (2021) 617–620.
[159] M. Tamagnone, K. Chaudhary, et al., ArXiv:1905.02177 (2019).
[160] J.D. Caldwell, A.V. Kretinin, et al., Nat. Commun. 5 (2014) 5221.
[161] M. Tamagnone, A. Ambrosio, et al., Sci. Adv. 4 (2018) 7189.
[162] P. Li, X. Yang, et al., Nat. Mater. 15 (2016) 870–875.
[163] K. Chaudhary, M. Tamagnone, et al., Nat. Commun. 10 (2019) 4487.
[164] T. Folland, A. Fali, et al., in: Photonic Phononic Prop. Eng. Nanostructures IX, International Society for Optics and Photonics, 2019, p. 109271F.
[165] A.M. Dubrovkin, B. Qiang, et al., Nat. Commun. 11 (2020) 1863.
[166] A. Bylinkin, M. Schnell, et al., Nat. Photonics 15 (2021) 197–202.
[167] V.W. Brar, M.S. Jang, et al., Nano Lett. 14 (2014) 3876–3880.
[168] S. Dai, Q. Ma, et al., Nat. Nanotechnol. 10 (2015) 682–686.
[169] Y. Jia, H. Zhao, et al., ACS Photonics 2 (2015) 907–912.
[170] A. Kumar, T. Low, et al., Nano Lett. 15 (2015) 3172–3180.
[171] J.D. Caldwell, L. Lindsay, et al., Nanophotonics 4 (2015) 44–68.
[172] X. Lin, Y. Yang, et al., Proc. Natl. Acad. Sci. 114 (2017) 6717–6721.
[173] G.X. Ni, L. Wang, et al., Nat. Photonics 10 (2016) 244–247.
[174] A.M. Dubrovkin, B. Qiang, et al., Nat. Commun. 9 (2018) 1762.
[175] K. Chaudhary, M. Tamagnone, et al., Sci. Adv. 5 (2019) eaau7171.
[176] M.A. Huber, F. Mooshammer, et al., Nat. Nanotechnol. 12 (2016) 207–211.
[177] G. Cerullo, S. De Silvestri, Rev. Sci. Instrum. 74 (2003) 1–18.
[178] B. Stern, X. Ji, et al., Nature 562 (2018) 401–405.
[179] T.T. Luu, M. Garg, et al., Nature 521 (2015) 498–502.
[180] P.B. Corkum, F. Krausz, Nat. Phys. 3 (2007) 381–387.
[181] N. Kumar, S. Najmaei, et al., Phys. Rev. B 87 (2013) 161403.
[182] Y. Li, Y. Rao, et al., Nano Lett. 13 (2013) 3329–3333.
[183] L.M. Malard, T.V. Alencar, et al., Phys. Rev. B 87 (2013) 201401.
[184] H. Liu, Y. Li, et al., Nat. Phys. 13 (2017) 262–265.
[185] X. Xu, W. Yao, et al., Nat. Phys. 10 (2014) 343–350.
[186] K.F. Mak, K.L. McGill, et al., Science 344 (2014) 1489–1492.
[187] Y. Li, A. Chernikov, et al., Phys. Rev. B 90 (2014) 205422.
[188] K. He, N. Kumar, et al., Phys. Rev. Lett. 113 (2014) 26803.
[189] Z. Ye, T. Cao, et al., Nature 513 (2014) 214–218.
[190] K.F. Mak, K. He, et al., Nat. Mater. 12 (2012) 207–211.
[191] N. Yoshikawa, T. Tamaya, et al., Science 356 (2017) 736–738.
[192] X. Yin, Z. Ye, et al., Science 344 (2014) 488–490.
[193] G. Wang, X. Marie, et al., Phys. Rev. Lett. 114 (2015) 097403.
[194] K.L. Seyler, J.R. Schaibley, et al., Nat. Nanotechnol. 10 (2015) 407–411.
[195] E. Hendry, P.J. Hale, et al., Phys. Rev. Lett. 105 (2010) 097401.
[196] A. Säynätjoki, L. Karvonen, et al., Nat. Commun. 8 (2017) 893.
[197] J. Klein, J. Wierzbowski, et al., Nano Lett. 17 (2017) 392–398.
[198] J.W. You, S.R. Bongu, et al., Nanophotonics 8 (2019) 63–97.
[199] A. Autere, H. Jussila, et al., Adv. Mater. 30 (2018) 1705963.
[200] S.A. Mikhailov, Europhys. Lett. 79 (2007) 27002.
[201] S.A. Mikhailov, K. Ziegler, J. Phys. Condens. Matter 20 (2008) 384204.
[202] M.M. Glazov, JETP Lett. 93 (2011) 366–371.
[203] J.L. Cheng, N. Vermeulen, et al., New J. Phys. 16 (2014) 053014.
[204] S.Y. Hong, J.I. Dadap, et al., Phys. Rev. X 3 (2013) 021014.
[205] T. Jiang, D. Huang, et al., Nat. Photonics 12 (2018) 430–436.
[206] H. Rostami, M. Polini, Phys. Rev. B 93 (2016) 161411.
[207] L. Miao, Y. Jiang, et al., Photonics Res. 3 (2015) 214–219.
[208] G. Soavi, G. Wang, et al., Nat. Nanotechnol. 13 (2018) 583–588.
[209] I. Alonso Calafell, L.A. Rozema, et al., Nat. Nanotechnol. 16 (2021) 318–324.
[210] J.L. Cheng, N. Vermeulen, et al., Opt. Express 22 (2014) 15868–15876.
[211] Y.Q. An, F. Nelson, et al., Nano Lett. 13 (2013) 2104–2109.
[212] S. Wu, L. Mao, et al., Nano Lett. 12 (2012) 2032–2036.
[213] J.J. Dean, H.M. Van Driel, Appl. Phys. Lett. 95 (2009) 261910.
[214] V.A. Margulis, E.E. Muryumin, et al., J. Phys. Condens. Matter 25 (2013) 195302.
[215] Y.Q. An, J.E. Rowe, et al., Phys. Rev. B 89 (2014) 115310.
[216] S. Ha, N.H. Park, et al., Light Sci. Appl. 10 (2021) 19.
[217] F. Yang, W. Song, et al., Matter 3 (2020) 1361–1376.
[218] K.H. Lin, S.W. Weng, et al., Appl. Phys. Lett. 105 (2014) 151605.
[219] Y. Zuo, W. Yu, et al., Nat. Nanotechnol. 15 (2020) 987–991.
[220] J.L. Krause, K.J. Schafer, et al., Phys. Rev. Lett. 68 (1992) 3535–3538.
[221] S. Ghimire, A.D. DiChiara, et al., Nat. Phys. 7 (2011) 138–141.
[222] Y.S. You, D.A. Reis, et al., Nat. Phys. 13 (2016) 345–349.
[223] O. Schubert, M. Hohenleutner, et al., Nat Phot. 8 (2014) 119–123.
[224] G. Ndabashimiye, S. Ghimire, et al., Nature 534 (2016) 520–523.
[225] N. Tancogne-Dejean, A. Rubio, Sci. Adv. 4 (2018) eaao5207.
[226] T. Tamaya, A. Ishikawa, et al., Phys. Rev. Lett. 116 (2016) 016601.
[227] T. Tamaya, A. Ishikawa, et al., Phys. Rev. B 94 (2016) 241107.
[228] A. Chernikov, T.C. Berkelbach, et al., Phys. Rev. Lett. 113 (2014) 76802.
[229] N. Yoshikawa, K. Nagai, et al., Nat. Commun. 10 (2019) 3709.
[230] G. Le Breton, A. Rubio, et al., Phys. Rev. B 98 (2018) 165308.
[231] Q. Bao, H. Zhang, et al., Adv. Funct. Mater. 19 (2009) 3077–3083.
[232] T. Hasan, Z. Sun, et al., Adv. Mater. 21 (2009) 3874–3899.
[233] S. Kivistö, T. Hakulinen, et al., Opt. Express 17 (2009) 2358.
[234] P.A. George, J. Strait, et al., Nano Lett. 8 (2008) 4248–4251.
[235] G.N. Ostojic, S. Zaric, et al., Phys. Rev. Lett. 92 (2004) 117402–117411.
[236] Y. Tan, X. Liu, et al., ACS Photonics 4 (2017) 1531–1538.
[237] J. Ma, G.Q. Xie, et al., Opt. Lett. 37 (2012) 2085–2087.
[238] A.A. Lagatsky, Z. Sun, et al., Appl. Phys. Lett. 102 (2013) 013113.
[239] J. Ma, G. Xie, et al., Sci. Rep. 4 (2014) 5016.
[240] M.N. Cizmeciyan, J.W. Kim, et al., Opt. Lett. 38 (2013) 341–343.
[241] N. Tolstik, A. Pospischil, et al., Opt. Express 22 (2014) 7284–7289.
[242] N. Tolstik, E. Sorokin, et al., Opt. Express 22 (2014) 5564–5571.
[243] W.B. Cho, S.Y. Choi, et al., Opt. Express 24 (2016) 20774–20780.
[244] J. Ma, G. Xie, et al., IEEE J. Sel. Top. Quantum Electron. 21 (2015) 1100806.
[245] G. Zhu, X. Zhu, et al., IEEE Photon. Tech. Lett. 28 (2016) 28–31.
[246] S.C. Xu, B.Y. Man, et al., Opt. Laser Technol. 56 (2014) 393–397.
[247] J. Liu, Y.G. Wang, et al., Laser Phys. Lett. 9 (2012) 15–19.
[248] Z. Qin, G. Xie, et al., Opt. Lett. 41 (2016) 56–59.
[249] J.F. Li, H.Y. Luo, et al., Sci. Rep. 6 (2016) 11.
[250] Z. Sun, A. Martinez, et al., Nat. Photonics 10 (2016) 227–238.
[251] C. Wei, X. Zhu, et al., Opt. Lett. 38 (2013) 3233–3236.
[252] Z. Qin, G. Xie, et al., Opt. Express 23 (2015) 24713–24718.
[253] G. Wang, Z. Wang, et al., Adv. Mater. 33 (2021) 2004070.
[254] S. Li, Y. Yin, et al., Opt. Express 27 (2019) 19843–19851.
[255] Z. Yang, L. Han, et al., Infrared Phys. Technol. 104 (2020) 103155.
[256] X. Tian, H. Luo, et al., Adv. Mater. 30 (2018) 1801021.
[257] H. Luo, X. Tian, et al., Photonics Res. 6 (2018) 900–907.
[258] J. Wang, J. Wei, et al., Appl. Opt. 59 (2020) 9165–9168.
[259] J. Yi, L. Du, et al., 2D Mater. 6 (2019) 045038.
[260] Q. Hao, J. Liu, et al., Appl. Phys. Express 12 (2019) 85506.
[261] R.R. Nair, P. Blake, et al., Science 320 (2008) 1308–1308.
[262] J.D. Cox, A. Marini, et al., Nat. Commun. 8 (2017) 14380.
[263] J. Wei, Z. Ren, et al., J. Appl. Phys. 128 (2020) 240901.
[264] M.-W. Chen, D. Ovchinnikov, et al., ACS Nano 11 (2017) 6355–6361.
[265] D.H. Lee, Y. Sim, et al., APL Mater. 8 (2020) 030901.
[266] A.A. Balandin, D.L. Nika, Mater. Today 15 (2012) 266–275.
[267] S.H. Lee, M. Choi, et al., Nat. Mater. 11 (2012) 936–941.

[268] T. Mueller, F. Xia, et al., Nat. Photonics 4 (2010) 297–301.
[269] M. Freitag, T. Low, et al., Nat. Commun. 4 (2013) 1951.
[270] B.Y. Zhang, T. Liu, et al., Nat. Commun. 4 (2013) 1811.
[271] F. Wang, L. Li, et al., Adv. Funct. Mater. 28 (2018) 1802707.
[272] H. Huang, J. Wang, et al., Nanotechnology 27 (2016) 445201.
[273] S.-Y. Xu, Q. Ma, et al., Nat. Phys. 14 (2018) 900–906.
[274] H. Xu, J. Wu, et al., Small 10 (2014) 2300–2306.
[275] Y. Liu, B.N. Shivananju, et al., ACS Appl. Mater. Interfaces 9 (2017) 36137–36145.
[276] L. Ye, H. Li, et al., ACS Photonics 3 (2016) 692–699.
[277] Q. Wang, Y. Wen, et al., Sci. Adv. 4 (2018) eaap7916.
[278] Z. Qin, T. Hai, et al., Opt. Express 26 (2018) 8224–8231.